Theoretical study of coalescence of bubbles in magma

丸石, 崇史

https://hdl.handle.net/2324/6787419

出版情報：Kyushu University, 2022, 博士（理学）, 課程博士
バージョン：
権利関係：

Doctoral Thesis

Theoretical study of coalescence of bubbles in magma

Takafumi MARUISHI

Kyushu Univ

Abstract

This thesis presents a theoretical study of the bubble coalescence in magma during volcanic eruptions. The study provides new insights into the understanding of bubble size distribution in pyroclasts and the bubble dynamics in conduit.

First, the interaction of two deformable bubbles under buoyancy is studied. The equation of motion for bubbles is formulated involving the effect of deformation. The calculation of the trajectory and shape reveals that the mechanism of attraction of two deformed bubbles under buoyancy. One bubble deforms due to the shear stress of the flow created by the ascending motion of the other bubble. This shape anisotropy leads to the incline of the ascending direction to the other bubble, resulting in attraction.

Next, the coalescence of spherical bubbles driven by buoyancy, shear, and growth is studied. The trajectory calculation reveals the critical conditions for bubble coalescence. The collision frequency functions for various driving forces are analytically obtained. These newly-derived functions are applicable to estimate the bubble coalescence during eruption.

Third, the evolution of the bubble size distribution is numerically studied. The evolution of the shape and moments of the size distribution are comprehensively studied. I find that, for buoyancy, shear, viscosity-limited growth, and isothermal expansion, the size distribution becomes power-law with a slope of -2 in a short time. I also find that, for diffusion-limited growth, the size distribution becomes power-law with a slope of -0.5. The empirical formulas for the shape and moments of the size distribution are provided.

Finally, bubble coalescence during volcanic eruption is discussed. For bubble in the depth of $2-6$ km during eruption, bubble can coalesce driven by diffusion-limited growth and viscosity-limited growth. This would impose constraints on the power-law seen in the bubble texture of pyroclasts. For basaltic eruption, the

bubbles over $0.1\ \mathrm{mm}$ can rapidly coalesce, forming large bubbles. The bubbles over $1\ \mathrm{cm}$ can more rapidly coalesce within $10\ \mathrm{sec}$ due to the effect of deformation. These coalescences may induce migration of bubbles and spatial inhomogeneity of gas in conduit. This may trigger the transition of eruption styles, such as the transition between Hawaiian and Stromblian eruptions.

Contents

Chapter 1

Introduction

1.1 Vesicualation of magma in volcanic eruption

Volcanic eruption starts from nucleation of sub-micron-sized bubbles in a magma chamber. Such bubbles grow by diffuion of volatiles contents from surrounding melts, and exapand by decompression as magma ascending to the surface. The expanding bubbles drive the eruption through accelerating the ascending magma, and would fracture the surrounding magma into discrete fragments, called pyroclasts. The presence of bubbles also significantly change the rheology of the magma, such as viscosity and yield strength. The vesicualtion of magma is thus a crucial factor controlling the eruption intensity and style.

Pyroclasts records the eruption dynamics as their bubble texture. Many textural studies have reported the morphological variables of the bubbles in pyroclasts, involving bubble number density, volume fraction of bubbles (vesicularity), and bubble size distribution. To interpret these bubble textures, theoretical models of vesicualtion has been developed (e.g; Toramaru, 1995)[1]. These theories describe the bubble dynamics under decompression including nucleation, growth, and expansion, giving the relation between the bubble number density and the ascending velocity of magma during eruption. This relation is useful tool to infer the conduit dynamics, which is difficult to observe directly, from the texture of pyroclasts.

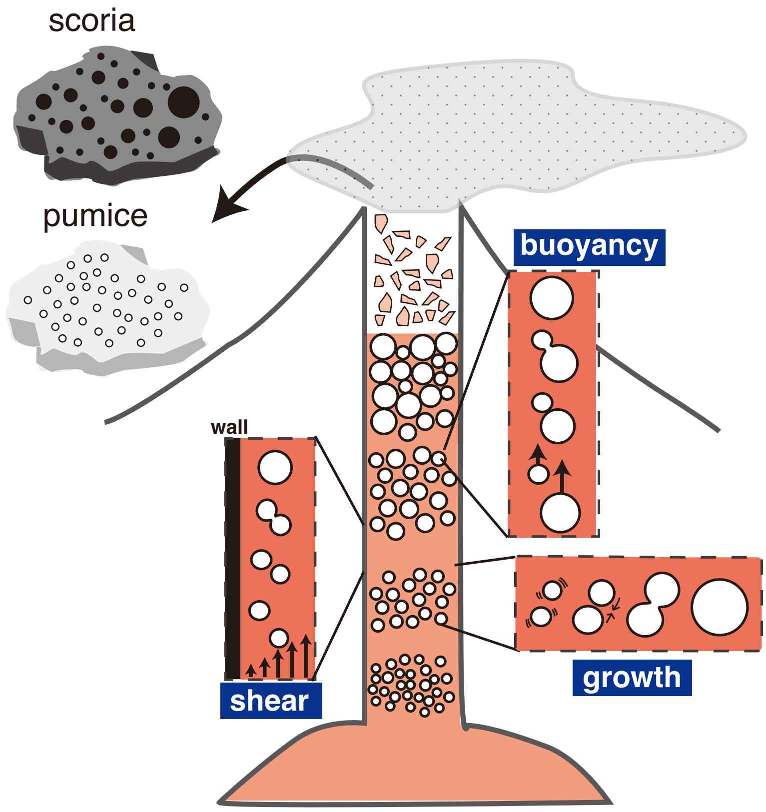

Fig. 1.1: A schematic illustration of bubble coalescence during eruption.

1.2 Bubble coalescence during eruption

Fig. 1.1 shows the illustration of bubble coalescence during eruption. The vesiculation involves coalescence as well as growth by volatile diffusion and expanding by decompression. Bubble coalescence makes the bubble size distrbituion polydisperse (having variation in size), reducing the bubble number density and increasing the averaged size of bubbles. The bubble size distribution controls the rheology of magma and criteria of the magma fragmentation. Thus bubble coalescence strongly affect the explosivity of the eruption. Considering coalescence of bubbles is crucial for understanding eruption dynamics and performing textural analysis.

Actually, many pyroclasts with texture of polydisperse bubbles are found, in-

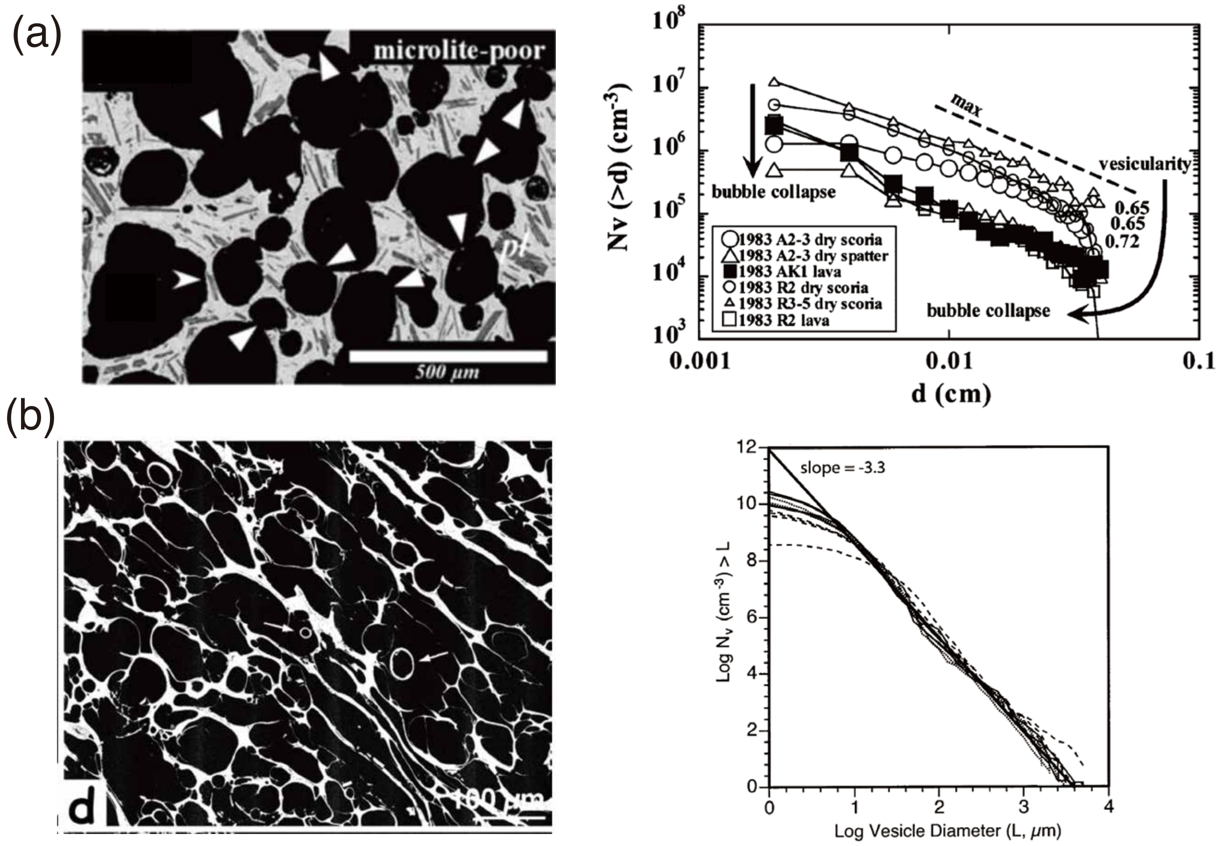

Fig. 1.2: (a) Bubble texture (left) and bubble size distribtuion (right) of scoria in 1983eruption of Miyakejima (Shimano and Nakada, 2006)[2]. (b) pumice in Mt.Mazama (Klug and Cashman, 2002)[3].

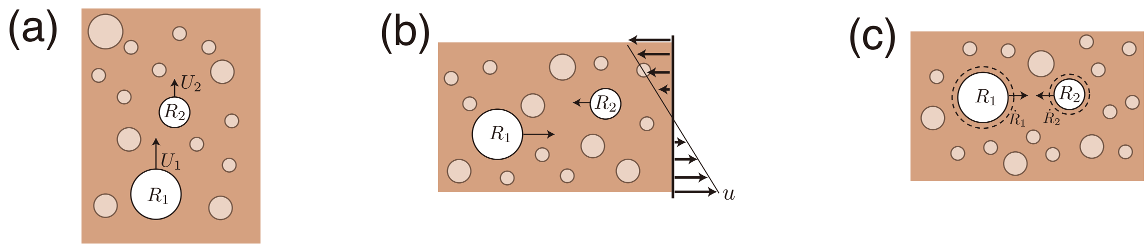

Fig. 1.3: Schematic illustration of the coalescence of two bubbles with radii R_1 and R_2. (a) Coalescence by ascending motion: bubble i ascends at the velocity of U_i. (b) Coalescence by simple shear flow. (c) Coalescence by growth or expansion.

dicating the interaction and coalescence of the bubbles (Fig. 1.2). The appearance of coalesced bubbles seem to depend on magma viscosity. In scoria, bubbles tend to retain a spherical shape, while in pumice they may have a stretched or connected appearance. These coalesced bubble structures often exhibit a wide power-law distribution in bubble size, with a range of over two orders of magnitude in radius.

1.3 Smoluchowski's theory of bubble coalescence

The bubble size distribution (BSD) of vesiculated magma becomes wider over time due to the growth and coalescence of bubbles. Various mechanisms contributes to bubble coalescence, including ascending motion, shear deformation, and decompression growth. Pyroclasts exhibits different size distributions depending on eruption conditions, ranging from narrow distributions such as exponential laws to wide distributions such as power laws [4]. A theoretical study of the evolution of BSD by bubble coalescence can improve understanding of bubble textures in pyroclasts and develop models of eruption dynamics.

The Smoluchowski coagulation equation is effective for describing the aggregation of particles by collision, such as the growth and coalescence of raindrops in clouds. The equation assumes that BSD evolves through repeated collisions and coalescences between two particles, which are characterized by a collision-frequency function. There have been few theoretical studies of bubble coalescence in magma using this equation. Sahagian (1989)[5] studied the coalescence and migration of ascending bubbles in lava. Gaonach et al. (1996)[6][7] and Lovejoy et al. (2004)[8] investigated the mathematical properties of power-law BSD due to coalescence. Mancini et al. (2016)[9] developed a numerical model that accounts for coalescence due to buoyancy and bubble growth. Unfortunately, a comprehensive understanding of BSD evolution through coalescence remains elusive due to the diversity of the driving forces and the higher nonlinearity of the Smoluchowski equation.

I briefly introduce the collision-frequency function that characterizes the collision of two bubbles. Let n_i denote the number of bubbles with radius R_i per unit volume, and let J_{12} denote the frequency of collision between bubble 1 and bubble 2 per unit time. The condition for two bubbles to collide is mathematically equivalent to a point of zero size colliding with a sphere of radius $R_1 + R_2$ at the origin. I denote the collisional area on the sphere at the origin where the points from infinity could inject as S_{col}. The collision rate J_{12} can be expressed as $J_{12} \sim n_1 n_2 S_{\mathrm{col}} \Delta U_{12}$, where S_{col} depends on the specifics of the problem. Fig. 1.3 schematically illustrates the bubble coalescence for three different conditions: (a) buoyancy, (b) shear, and (c) bubble growth.

1.4 Problems of the bubble coalescence model

1.4.1 Hydrodynamic interaction

One reason for the lack of theoretical models for bubble coalescence is the complexity of bubble interaction in magma. Moving or expanding bubbles create a flow around them, which causes the interaction between the bubbles. Bubbles are inevitably subjected to such interaction induced by the surrounding magma because magma is highly viscous liquid. Manga and Stone (1994)[10] experimentally found that small bubbles are repulsive each other, while large bubbles deform and attract each other (Fig. 1.4). They measured these interaction as the collision efficiency and showed that such hydrodynamic interaction significantly changes the collision efficiency. However, the collision efficiency is measured only in a limited range of the bubble sizes for buoyant motion of bubbles. It is needed to determine the collision efficiency over a wide range of bubble sizes for various driving forces as well as buoyancy.

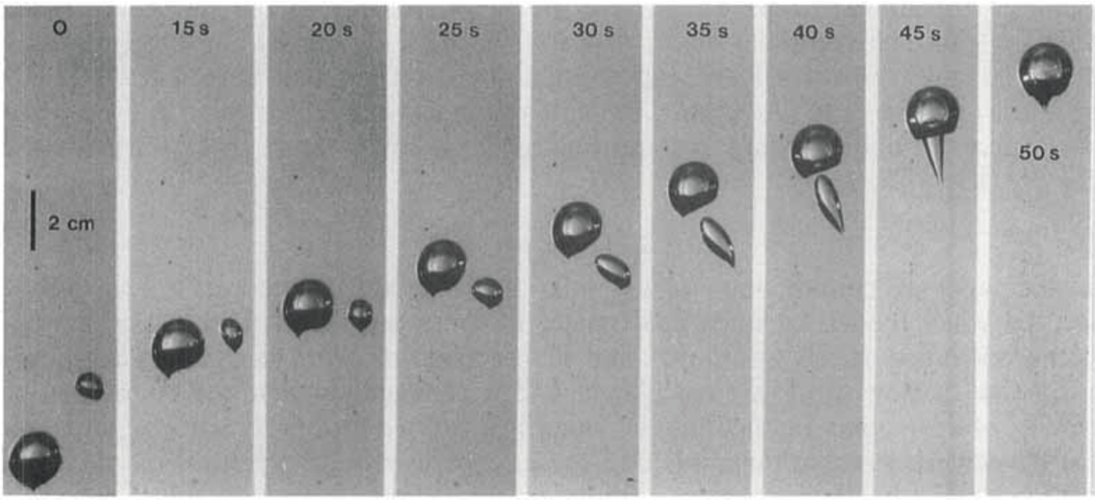

Fig. 1.4: Bubble interaction in viscous liquid (Manga and Stone, 1994)[10].

1.4.2 Evolution of distribution shape and moments

In volcanic eruptions, bubble coalescence is driven by various factors, including buoyancy, shear, and growth. Experimental studies have reported that bubble coalescence leads to a power-law BSD [11]. However, the parameters that control the shape of the BSD during bubble coalescence remain unclear. Therefore, the evolution of the bubble number density and the vesicularity, which are essential quantities for textural analysis of pyroclasts and modeling of the eruption dynamics, are not well understood.

1.5 Aim of this study

In this study, I aim to develop a new theory of bubble coalescence. Using this theory, I will investigate the evolution of the size distribution of bubbles due to coalescence and clarify the shape and time scale of the distribution. This will be useful for advancing volcanic conduit dynamics models and interpreting experimental and natural results. Our goal is to understand the dynamics of bubble coalescence during volcanic eruption.

Chapter 2

Coalescence of two deformable bubbles ascending in viscous liquid

This chapter is based on a published paper, Maruishi and Toramaru (2022)[12]. The goal of this chapter is to clarify the interaction and coalescence of deformable bubbles under buoyancy. I formulate the equations of motion for the positions and shapes of the bubbles. In this formulation, a bubble ascends with a velocity that depends on its shape. Solving the equations, I investigate how two ascending bubbles interact in a simple configuration. As a result, I clarify the condition that determines whether the two bubbles collide in terms of the two dimensionless parameters Bo and λ. From the scaling argument with the experimental data, I develop a new model for the cross-section for coalescence of deformable bubbles applicable for the wide Bo range. Our model provides more reasonable estimations than the empirical model of Manga and Stone[10],[13].

2.1 Equation of motion of deformable bubbles

I formulate the equations of motion for two deformable bubbles in a viscous liquid based on the work of Saintillan et al.[14]. Similarly to their work, I made the following two assumptions to simplify the interaction, with the bubbles sufficiently separated: (i) The disturbance flow caused by one deformed bubble A near the other bubble B is approximated as the flow created by the motion of a spherical bubble A, neglecting the deformation of the bubble A; and (ii) the disturbance flow inducing a deformation of bubble B is treated as a linear shear flow.

Hereafter, the index $i = 1$ denotes the trailing bubble and $i = 2$ denotes the leading bubble. Bubble i with central position $\boldsymbol{x}_i$ has a radius R_i when it is spherical. The surrounding liquid's density and viscosity are ρ and μ. The interfacial tension between the bubbles and the surrounding liquid is σ.

I consider that the bubbles are in the linear ambient field given as:

$$\boldsymbol{u}^{\infty}(\boldsymbol{x}) = \boldsymbol{E}^{\infty} \cdot \boldsymbol{x} + \boldsymbol{\Omega}^{\infty} \times \boldsymbol{x} \tag{2.1}$$

where $\boldsymbol{E}^{\infty}$ is the rate-of-strain tensor, which is symmetric and traceless, and $\boldsymbol{\Omega}^{\infty}$ is the rigid-rotation tensor, which is antisymmetric. I consider that the bubbles are subjected to buoyant forces proprotional to their volumes:

$$\boldsymbol{F}_i = \frac{4\pi}{3}\rho g R_i^3 \boldsymbol{e}_z \tag{2.2}$$

I assume that the shape of a bubble is approximated by a small deformed ellipsoid, whose surface is defined by:

$$r_i(\boldsymbol{n}) = R_i \left(1 + \boldsymbol{n} \cdot \boldsymbol{A}_i \cdot \boldsymbol{n}\right) \tag{2.3}$$

where $r_i(\boldsymbol{n})$ is the radial distance from the center to the interface of bubble i in the direction of a unit vector $\boldsymbol{n}$, $\boldsymbol{A}_i$ is the shape tensor for bubble i and is a symmetric and traceless second-order tensor describing the direction and length of the axes of the ellipsoidal bubble. Under assumption (ii), the evolution of $\boldsymbol{A}_i$ is described by small deformation theory[15]:

$$\frac{d\boldsymbol{A}_i}{dt} = \left\{\left(\boldsymbol{\Omega}^{\infty} + \boldsymbol{\Omega}_j(\boldsymbol{x}_i)\right)\boldsymbol{A}_i - \boldsymbol{A}_i\left(\boldsymbol{\Omega}^{\infty} + \boldsymbol{\Omega}_j(\boldsymbol{x}_i)\right)\right\} + \frac{5}{3}\left(\boldsymbol{E}^{\infty} + \boldsymbol{E}_j(\boldsymbol{x}_i)\right) - \frac{5}{6}\frac{\sigma}{\mu R_i}\boldsymbol{A}_i \tag{2.4}$$

where $\boldsymbol{E}_j(\boldsymbol{x}_i),\ \boldsymbol{\Omega}_j(\boldsymbol{x}_i)$ are tensors for strain and rotation rates at the center of bubble i under the disturbance flow caused by the other bubble j $(\neq i)$, as given later. The first and second terms of the right-hand side describe rotation and elongation motions of bubble i under the ambient flow and the disturbance flow caused by bubble j. The last term describes relaxation of the shape of bubble i to a sphere by surface tension.

The translational velocity of bubble i is the linear sum of three contributions: the velocity of the ambient flow $\boldsymbol{u}^{\infty}$, the rising velocity of an isolated deformed bubble $\boldsymbol{U}_i$ and the velocity of the disturbance flow $\boldsymbol{u}_j$ caused by bubble j as follows:

$$\frac{d\boldsymbol{x}_i}{dt} = \boldsymbol{u}^{\infty}(\boldsymbol{x}_i) + \boldsymbol{U}_i + \boldsymbol{u}_j(\boldsymbol{x}_i) \tag{2.5}$$

$\boldsymbol{U}_i$ is the product of the viscous mobility matrix $\boldsymbol{M}_i$ and the buoyancy force $\boldsymbol{F}_i$.

$$\boldsymbol{U}_i = \boldsymbol{M}_i \boldsymbol{F}_i \tag{2.6}$$

$\boldsymbol{M}_i$ is the sum of the contributions from spherical and non-spherical shapes[16]:

$$\boldsymbol{M}_i = \frac{1}{4\pi R_i \mu}\left(\boldsymbol{I} + \frac{2}{5}\boldsymbol{A}_i\right) \tag{2.7}$$

where $\boldsymbol{I}$ is an identity matrix representing the contribution of the spherical shape and $\frac{2}{5}\boldsymbol{A}_i$ is the effect of non-spherical shapes.

2.2 Setup

Thus, the rate of strain $\boldsymbol{E}_j$ and rotation Ω_j of the disturbance flow $\boldsymbol{u}_j$ are calculated as follows:

$$\begin{aligned}
\boldsymbol{E}_j(\boldsymbol{x}) &= (\nabla \boldsymbol{u} + \nabla \boldsymbol{u}^T)/2 \\
&= -\frac{R_j U_{s,j}}{2|\boldsymbol{x} - \boldsymbol{x}_j|^2}(\boldsymbol{e}_r \cdot \boldsymbol{e}_z)(\boldsymbol{I} - 3\boldsymbol{e}_r\boldsymbol{e}_r) && (2.8) \\
\boldsymbol{\Omega}_j(\boldsymbol{x}) &= (\nabla \boldsymbol{u} - \nabla \boldsymbol{u}^T)/2 \\
&= -\frac{R_j U_{s,j}}{2|\boldsymbol{x} - \boldsymbol{x}|^2}(\boldsymbol{e}_z\boldsymbol{e}_r - \boldsymbol{e}_r\boldsymbol{e}_z) && (2.9)
\end{aligned}$$

The bubbles approach each other due to the difference in ascent velocity and the attraction effect of deformation. Manga and Stone[10]'[13] experimentally reported that the bubbles follow the three types of trajectory: (a) 'coat', where the larger bubble collides with the small bubble from below and they coalesce, (b) 'entrain', where the larger bubble does not collide initially and pass through and moves above the smaller bubble, then they collide and coalesce, and (c) 'miss', where the two bubbles do not collide. The trajectory type changes from 'coat' to 'entrain' and to 'miss' as the initial horizontal separation x_0 increases (Fig. 2.1).

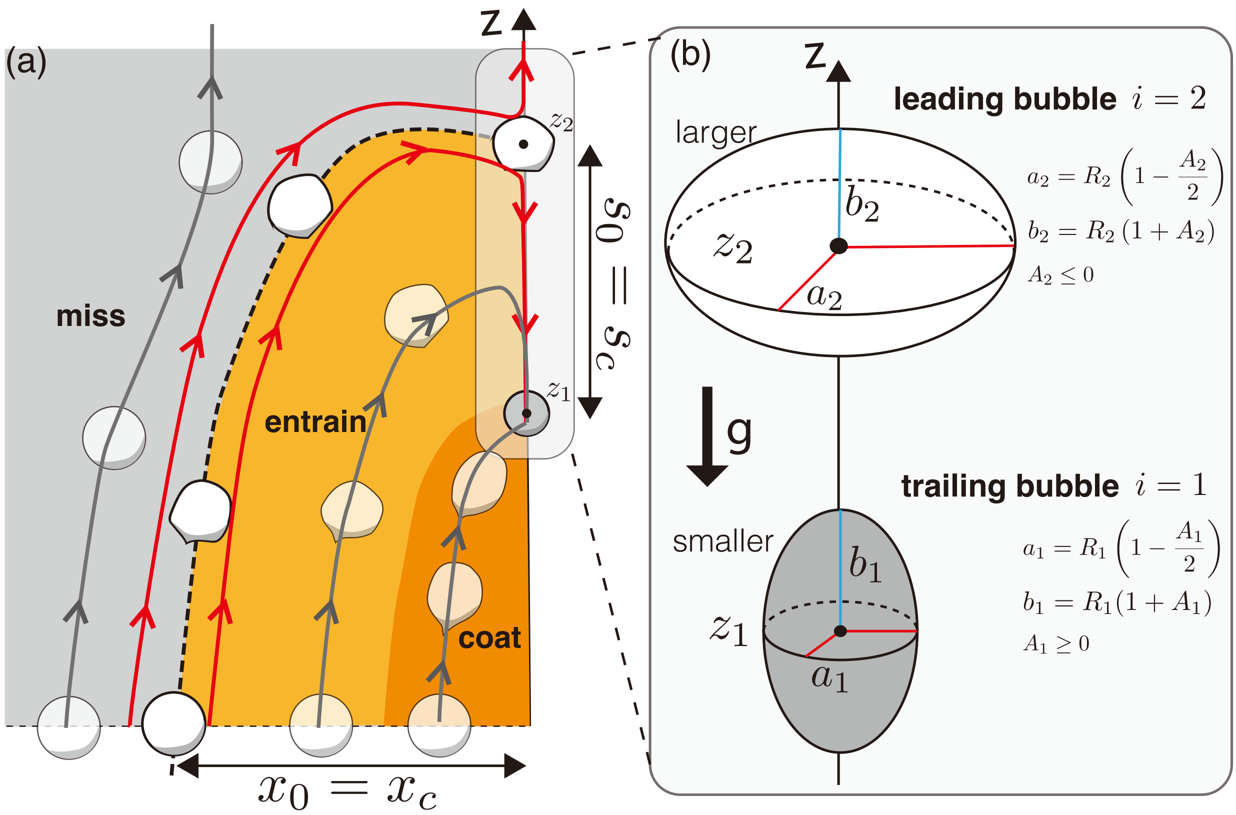

Fig. 2.1: (a) Illustration of relative trajectories in the reference frame of a small trailing bubble located at z_1. Along the dashed boundary line between 'entrain' and 'miss', the bubbles have an initial horizontal separation of x_0 and a vertical separation of s_0 just after they align along the vertical axis z. (b) Geometry of the two bubbles in the vertical axis. The deformed bubbles have a vertical length $R_i(1 + A_i)$ and a horizontal length $R_i(1 - A_i/2)$ $(i = 1, 2)$. The leading bubble is larger than the trailing bubble $R_1 < R_2$.

Thus, a critical condition for bubble coalescence exists in 'entrain' regime. The trajectory type also depends on two dimensionless parameters, the size ratio λ and Bo. The same shift in trajectory occurs as λ and Bo decreases. To focus on the 'entrain' regime, I limit the dimensionless parameters to the ranges $0.2 < \lambda$ and $10 < \mathrm{Bo}$.

To determine the conditions for bubble coalescence, I focus on the trajectories around the boundary between 'entrain' and 'miss' illustrated as blue lines in Fig. 2.1(a). In these trajectories, the two bubbles align vertically before they separate or collide. Thus, I formulate the relative vertical motion of the two bubbles and determine the critical vertical separation s_c. After that, I convert s_c to the critical horizontal separation x_c. Note that the initial vertical positions of the two bubbles are inverted after they align, as the larger bubble is located above the smaller bubble [Fig. 2.1(b)].

If I assume that the bubbles are initially on the z axis and have axisymmetric shapes [Fig. 2.1(b)], the bubbles remain on the z axis and keep their axisymmetric shapes. Under the initial condition, the position vector $\boldsymbol{x_i}$ and $\boldsymbol{A}_i$ are as follows:

$$\boldsymbol{x}_i = \begin{pmatrix} 0 \\ 0 \\ z_i \end{pmatrix} \tag{2.10}$$

$$\boldsymbol{A}_i = \begin{pmatrix} -A_i/2 & 0 & 0 \\ 0 & -A_i/2 & 0 \\ 0 & 0 & A_i \end{pmatrix} \tag{2.11}$$

where the diagonal component A_i is referred to as the shape index.

Here, I define the vertical separation between the two bubbles for describing the relative motion:

$$s = z_2 - z_1 \tag{2.12}$$

The position of the origin of the vertical axis z has no influence on the trajectory calculation.

The disturbance flow $\boldsymbol{u}_j$, the strain rate $\boldsymbol{E}_j$, and the rotation rate Ω_j in the shape evolution equation (2.4) are evaluated using (3.15)–(2.9) as follows:

$$u_j(\boldsymbol{x}_i) = \frac{U_{s,j}}{s}\begin{pmatrix}0\\0\\1\end{pmatrix} \tag{2.13}$$

$$\boldsymbol{E}_j(\boldsymbol{x}_i) = (-1)^i \frac{R_j U_{s,j}}{2s^2}\begin{pmatrix}-1 & 0 & 0\\ 0 & -1 & 0\\ 0 & 0 & 2\end{pmatrix} \tag{2.14}$$

$$\Omega_j(\boldsymbol{x}_i) = O \tag{2.15}$$

The original equations of motion (2.4) and (2.5) can be reduced to equations in terms of the vertical separation s and the shape indices of the two bubbles $A_1,\ A_2$ using (2.6)–(2.11) as follows:

$$\frac{dz_1}{dt} = U_{s,1}\left(1+\frac{2}{5}A_1\right) + \frac{R_2 U_{s,2}}{s} \tag{2.16}$$

$$\frac{dz_2}{dt} = U_{s,2}\left(1+\frac{2}{5}A_2\right) + \frac{R_1 U_{s,1}}{s} \tag{2.17}$$

$$\frac{ds}{dt} = U_{s,2} - U_{s,1} - \frac{2}{5}\left(A_1 U_{s,1} - A_2 U_{s,2}\right) + \frac{R_1 U_{s,1} - R_2 U_{s,2}}{s} \tag{2.18}$$

$$\frac{dA_1}{dt} = \frac{5}{3}\frac{R_2 U_{s,2}}{s^2} - \frac{5}{6}\frac{\sigma}{\mu R_1}A_1 \tag{2.19}$$

$$\frac{dA_2}{dt} = -\frac{5}{3}\frac{R_1 U_{s,1}}{s^2} - \frac{5}{6}\frac{\sigma}{\mu R_2}A_2 \tag{2.20}$$

The relative velocity $\frac{ds}{dt}$ is the sum of three contributions: separation motion due to the difference in the ascent velocities of the spherical bubbles $U_{s,1} - U_{s,2}$, attraction motion as the velocity correction for the deformed shape of the bubbles $\frac{4}{5}(A_2 U_{s,2} - A_1 U_{s,1})$, and attraction motion due to the disturbance flow induced by the ascending motion of the two bubbles $\frac{R_1 U_{s,1} - R_2 U_{s,2}}{s}$.

I non-dimensionalize the governing equation using the typical scales, the averaged radius of the two bubbles, and the ascent velocity of bubbles 2 that is isolated and spherical:

$$\text{length scale :}\frac{R_1 + R_2}{2} \tag{2.21}$$

$$\text{velocity scale :}U_{s,2} \tag{2.22}$$

The non-dimensionalized equations are as follows:

$$\frac{ds^*}{dt^*} = 1 - \lambda^2 - \frac{2}{5}(\lambda^2 A_1 - A_2) - \frac{2(1-\lambda^3)}{1+\lambda}\frac{1}{s^*} \tag{2.23}$$

$$\frac{dA_1}{dt^*} = \frac{10}{3}\frac{1}{1+\lambda}\frac{1}{s^{*2}} - \frac{5}{4}\frac{1+\lambda}{\lambda \mathrm{Bo}}A_1 \tag{2.24}$$

$$\frac{dA_2}{dt^*} = -\frac{10}{3}\frac{\lambda}{1+\lambda}\frac{1}{s^{*2}} - \frac{5}{4}\frac{1+\lambda}{\mathrm{Bo}}A_2 \tag{2.25}$$

where $s^* = \frac{2s}{R_1+R_2}$ and $t^* = \frac{2U_{s1}t}{R_1+R_2}$ are the non-dimensionalized separation and time. Equations (2.23)–(2.25) have two dimensionless parameters, Bo and λ:

$$\mathrm{Bo} = \frac{\rho g R_2^2}{\sigma} \tag{2.26}$$

$$\lambda = \frac{R_1}{R_2} \tag{2.27}$$

I assume that the Reynolds number defined by the averaged radius (2.21) and the ascent velocity of the larger bubble (2.22) is much smaller than unity:

$$\mathrm{Re} = \frac{\rho U_{s,2}\left(R_1+R_2\right)}{2\mu} \ll 1 \tag{2.28}$$

2.3 Results

2.3.1 Numerical calculation for 'coat' condition: comparison with laboratory experiment

To validate our model, I compared our calculations with the previous experiment on bubble coalescence for large Bond number $\mathrm{Bo} \approx 100$ by Manga and Stone[17]. This model can deal with the motion of bubbles aligned vertically. Both the 'entrain' and 'coat' conditions satisfy this situation. Because their work has no experiments for the 'entrain' condition, I use the behavior of 'coat' condition to validate our model.

To estimate the motion of the bubbles in the experiment, I detected the bubble interfaces in experimental photographs shown as orange curves in Fig.2.2(a). I used the photographs before collision $t \leq 25$ s, where the bubble interfaces are clearly defined. I estimated that the bubble radii are $R_1 = 1.2$ cm, $R_2 = 1.0$ cm, the initial separation is $s_0 = 5.9$ cm, and the ascent velocity is $U_1 = 0.3$ cm/s.

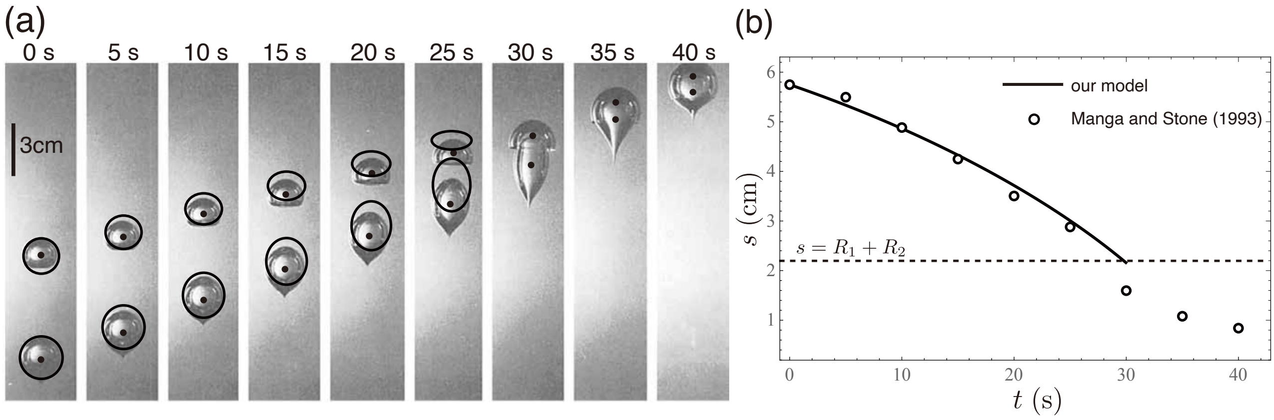

Fig. 2.2: Comparison of the bubble positions and shapes for the 'coat' condition by our calculation and the previous experiment of Manga and Stone[17]. $\mathrm{Bo} = 100,\ \lambda = 0.8,\ s_0^* = 5.4$. (a) Our calculation (black ellipses) overlaid with an experimental photograph before collision. The orange curves indicate the bubble interfaces in the experiment. The dots in the bubbles indicate their geometrical centers. (b) Evolution of the separation between the two bubbles. The solid line indicates our calculation. The open circles indicate the experimental data from the photograph. (c) Evolution of the shape indices of the two bubbles by our calculation.

Equations (2.23)–(2.25) were thus solved with $\mathrm{Bo} = 100,\ \lambda = 0.8,\ s_0^* = 5.4$, assuming that the bubbles are initially spherical for simplicity ($A_1 = A_2 = 0$ at $t^* = 0$). The calculation was stopped when the two bubbles touch at $s^* = 2$.

Figure 2.2(a) shows the motion of the bubbles by our calculation overlaid with the experimental photograph. The black ellipsoids represent the bubble interfaces by our calculation. The horizontal length a_i and the vertical length b_i of bubble i are calculated as shown in Fig 2.1(b):

$$a_i = R_i \left(1 - \frac{A_i}{2}\right) \tag{2.29}$$

$$b_i = R_i \left(1 + A_i\right) \tag{2.30}$$

Our calculations approximately reproduce the evolution of the centers and the shapes of the bubbles in the experiments. The geometrical centers calculated by our models are slightly higher than those in the experiment $t > 15$ s. Figure 2.2(b) compares the experimental and numerical calculation results for the evolution of bubble separation, which are seen to be in good agreement. Note that I used equations (2.23)–(2.25) even for large deformation $A_i \sim 1$.

2.3.2 Numerical calculation for 'entrain' condition

I calculated the motion of the bubbles for the 'entrain' condition where the larger leading and the smaller trailing bubbles align vertically [Fig. 2.1(b)]. The bubbles are assumed to be initially spherical ($A_1 = A_2 = 0$ for $t = 0$). The calculation was stopped when the two bubbles touch $s^* = 2$ or collapse $a_1 = 0,\ b_2 = 0$.

Figure 2.3(a) shows the evolution of the separation s obtained by numerically solving equations (2.23)–(2.25) for several initial separations s_0. The bubbles with an initial separation $s_0^* > 11$ move away from each other, resulting in no collision ($s^* \to \infty$). For an initial separation $s_0 < 11$, the bubble separation s^* initially increases and then decreases with time, and approaches $s^* = 2$, where it is believed that the two bubbles collide and coalesce. However, in these cases, the calculation was stopped before the separation reached $s^* = 2$ because the trailing bubble collapsed ($a_1 = 0$). I define the critical initial separation s_c as the smallest initial separation s_0 that results in no collision ($s^* \to \infty$). The critical initial separation in this case ($\mathrm{Bo} = 300,\ \lambda = 0.85$) is $s_c^* \simeq 11$.

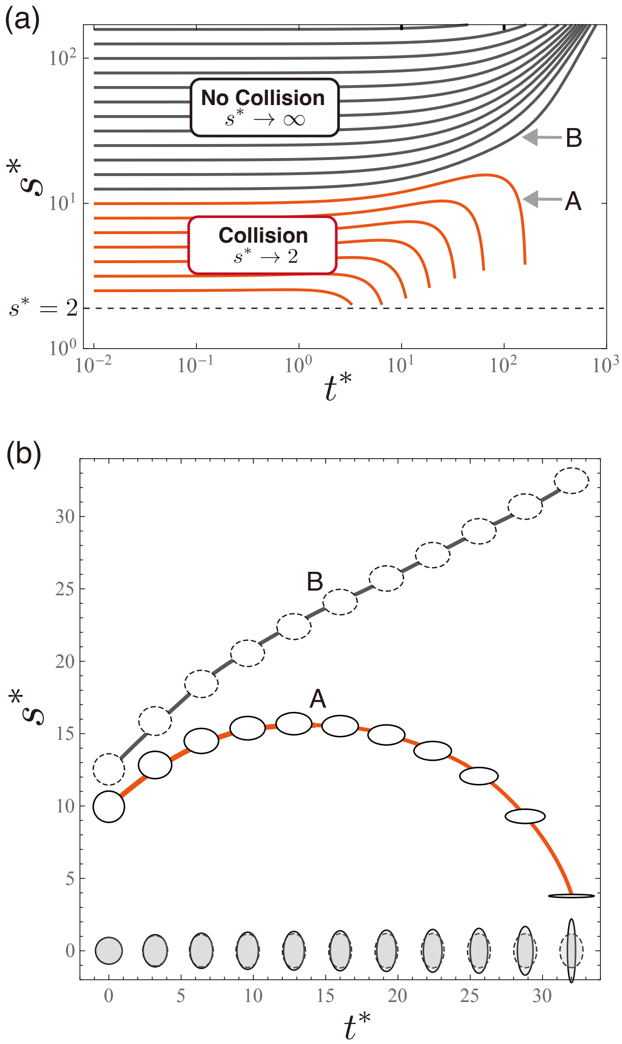

Fig. 2.3: (a) Evolution of the separation between the bubbles for $\mathrm{Bo} = 300,\ \lambda = 0.85$. The red lines indicate the trajectories resulting in collisions ($s^* \to 2$). The grey lines indicate the trajectories resulting in no collision ($s^* \to \infty$). (b) Evolution of the shape and separation of the bubbles for the two conditions resulting in collision (A) and no collision (B) as labeled in (a). The upper solid and dashed ellipses within the red and grey lines indicate the leading bubbles of A and B. The lower ellipses nearly overlapped represent the trailing bubbles of A and B.

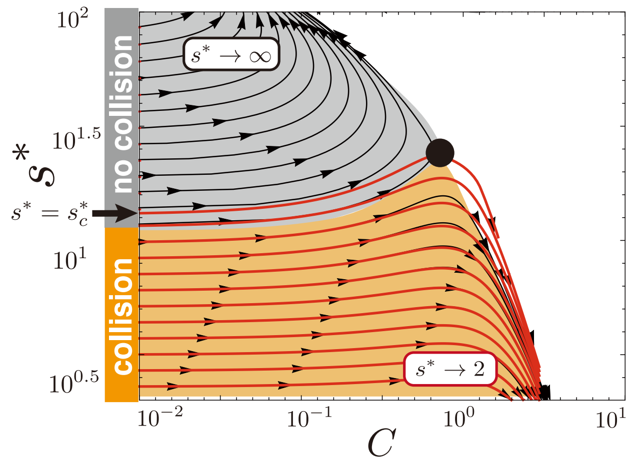

Fig. 2.4: Evolution of the shape and separation of the bubbles on the (C, s^*) plane for $\mathrm{Bo} = 300$, $\lambda = 0.85$. The black lines represent the solutions of the reduced equations of motion (2.32), (2.33). The arrows indicate the direction of time. The red lines represent the asymptotic solutions (2.35). The black circle represents the unstable point (2.34).

Figure 2.3(b) shows the evolution of the shape and separation of the bubbles for two trajectories A and B labeled in Fig. 2.3(a), where A has a slightly smaller initial separation than the critical separation ($s_0 < s_c$) and B has a slightly higher initial separation ($s_0 > s_c$). The evolution of the shapes of the trailing bubbles in A and B is almost the same. The leading bubble in A first moves away until $t^* \simeq 15$ and then approaches the trailing bubble, collapsing at $t^* \simeq 30$, whereas the leading bubble in B moves away from the trailing bubble.

2.3.3 Asymptotic analysis of the equations of motion

To clarify the conditions for which the bubbles collide, I performed an asymptotic analysis of the equations of motion for the bubbles (2.23)–(2.25). I consider two similar-sized bubbles $\lambda \simeq 1$ and neglect the hydrodynamic interaction $\frac{2(1-\lambda^3)}{1+\lambda}\frac{1}{s^*}$ in equation (2.23). I define the shape contrast C between the bubbles as:

$$C = A_1 - A_2 \tag{2.31}$$

For two spherical bubbles, $A_1 = 0$, $A_2 = 0$, and $C = 0$. For two deformed bubbles, as in Fig. 2.1(b), $A_1 > 0$, $A_2 < 0$, and $C > 0$. Then, equations (2.23)–

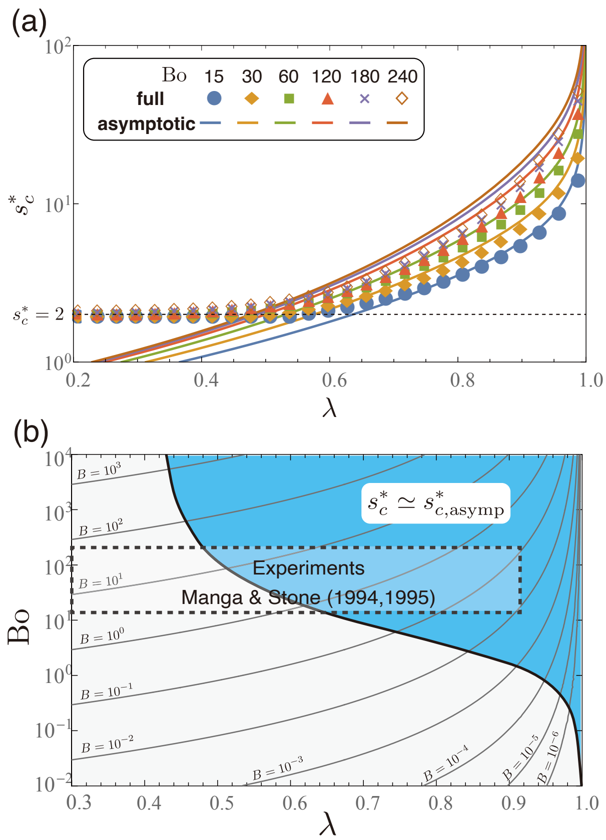

Fig. 2.5: (a) Comparison of the critical vertical separation by asymptotic and numerical calculations. The solid lines represent the asymptotic values using the asymptotic formula (2.38). The markers represent the numerical values obtained by solving the full equations (2.23)–(2.25). (b) Bond number and size ratio such that the asymptotic formula (2.38) holds $s_c^* \simeq s^*_{c,\mathrm{asymp}}$, indicated by the blue region. The blue region is determined by the inequality $s^*_{c,\mathrm{asymp}} \geq 2$. The gray lines represent the contours of rescaled Bond number. The dashed region represents the experimental parameter range of Manga and Stone[10],[13].

(2.25) are reduced to equations of motion for separation s^* and shape contrast C:

$$\frac{d}{dt^*}\left(\frac{1}{s^*}\right) = \frac{2}{5}s^{*-2}\left(C - \bar{C}\right) \tag{2.32}$$

$$\frac{dC}{dt^*} = \frac{10}{3}\frac{1}{s^{*2}} - \frac{5}{2\mathrm{Bo}}C \tag{2.33}$$

where $\bar{C} = 5(1-\lambda)$ represents the equilibrium value of the shape contrast satisfying $\frac{ds^*}{dt} = 0$ in equation (2.23) without the last term. It is noted that the effect of λ comes from $\bar{C}$.

Figure 2.4 shows the evolution of the shape and separation of the bubble motions as a black line on the $(C,\ s^*)$ plane. The trajectories are obtained by numerically solving the reduced equations (2.32) and (2.33) for $\mathrm{Bo} = 300,\ \lambda = 0.85$. The trajectory in the upper region results in collision, $s^* \to 2$, whereas the trajectory in the lower region results in no collision, $s^* \to \infty$. The black circle represents the unstable point at which the trajectory avoids passing:

$$\left(\bar{C},\ \frac{2}{\sqrt{3}}\frac{\mathrm{Bo}^{1/2}}{\bar{C}^{1/2}}\right) \tag{2.34}$$

which is obtained by setting the right-hand sides of (2.32) and (2.33) to zero. The trajectory passing the bottom side of the unstable point results in collision, whereas the trajectory passing the top side results in no collision.

I theoretically estimate s_c using an asymptotic solution. When the bubbles are initially spherical ($C = 0$), and the surface tension term $\frac{5}{2\mathrm{Bo}}C$ in (2.33) is neglected, the solution of (2.32) and (2.33) is given by:

$$s^*(C) = \left(\frac{3}{50}\left(C - \bar{C}\right)^2 + \frac{1}{s_0^*} - \frac{3}{2}(1-\lambda)^2\right)^{-1} \tag{2.35}$$

where s_0^* is the initial vertical separation. The asymptotic solutions are plotted in Fig. 2.4 as red lines, are convex upward. The maximum point of the solution is as follows:

$$\left(\bar{C},\ \left(\frac{1}{s_0^*} - \frac{3}{2}(1-\lambda)^2\right)^{-1}\right) \tag{2.36}$$

$s^*_{c,\mathrm{asymp}}$ is defined as s^*_0 for which the maximum point of the asymptotic curve (2.36) coincides with the unstable point (2.34):

$$\left(\frac{1}{s^*_{c,\mathrm{asymp}}} - \frac{3}{2}(1-\lambda)^2\right)^{-1} = \frac{2}{\sqrt{3}}\frac{\mathrm{Bo}^{1/2}}{\bar{C}^{1/2}} \tag{2.37}$$

As a result, $s^*_{c,\mathrm{asymp}}$ is determined as a function of Bo and λ as follows:

$$s^*_{c,\mathrm{asymp}}(\mathrm{Bo},\lambda) = \left(\frac{\sqrt{15}}{2}\frac{(1-\lambda)^{1/2}}{\mathrm{Bo}^{1/2}} + \frac{3}{2}(1-\lambda)^2\right)^{-1} \tag{2.38}$$

Multiplying both sides of this expression by $\mathrm{Bo}^{-2/3}$, I obtain the simplified expression:

$$S_{c,\mathrm{asymp}}(B) = \left(\frac{\sqrt{15}}{2}B^{1/6} + \frac{3}{2}B^{2/3}\right)^{-1} \tag{2.39}$$

where $S_{c,\mathrm{asymp}}$ is the rescaled critical vertical separation and B is the rescaled Bond number defined as:

$$S_{c,\mathrm{asymp}} = s^*_{c,\mathrm{asymp}}\mathrm{Bo}^{-2/3} \tag{2.40}$$

$$B = (1-\lambda)^3\mathrm{Bo} \tag{2.41}$$

In the derivation of the asymptotic formula for the critical vertical separation $s^*_{c,\mathrm{asymp}}$ (2.38), I used the reduced equations (2.32) and (2.33) assuming similar sizes for the two bubbles $\lambda \simeq 1$. To estimate the error of this approximation, I calculated s^*_c for different-sized bubbles by solving numerically the full equations (2.23)–(2.25). Figure 2.5(a) compares the asymptotic formula and the full calculation for $15 < \mathrm{Bo} < 240$. For $\lambda \gtrsim 0.5$, the asymptotic formula agrees with the full calculation. For $\lambda \lesssim 0.5$, the asymptotic formula disagrees with the full calculation, because the asymptotic curves are below the minimum $s^*_c = 2$. Figure 2.5(b) shows the parameters the asymptotic formula holds as the blue region determined by $s^*_{c,\mathrm{asymp}} \geq 2$.

2.4 Discussion

2.4.1 Cross-section for coalescence of deformable bubbles

The critical horizontal separation x_c is defined as the largest initial horizontal separation x_0 for which the bubbles coalesce [Fig. 2.1a]. In terms of the dimensionless

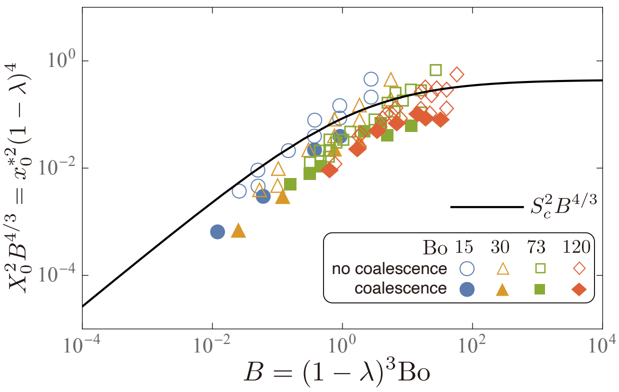

Fig. 2.6: Experimental results for whether the bubbles coalesce obtained by Manga and Stone[13] replotted with axes of rescaled Bond number B and square of the rescaled initial horizontal separation $X_0^2 B^{4/3}$. The open symbols indicate the case where the bubbles do not coalesce. The closed symbols indicate the case where the bubbles coalesce. The black line is the analytical curve for the critical vertical separation $\frac{1}{2}S_{c,\mathrm{asymp}}^2 B^{4/3}$ by equation (2.39).

variable scaled by $\pi(R_1 + R_2)^2$, the cross-section E^* is defined as the square of x_c^*:

$$E^* = \frac{1}{4}x_c^{*2} \tag{2.42}$$

As discussed in Section 2.3.3, I found that the rescaled critical vertical separation $S_{c,\mathrm{asymp}}$ is a function of the rescaled Bond number B, as expressed by equation (2.39). Similar to this result, I assume that the rescaled critical horizontal separation X_c is a function of B as follows:

$$X_c = x_c^* \mathrm{Bo}^{-2/3} \tag{2.43}$$

$$X_c = X_c(B) \tag{2.44}$$

Under this assumption, I use the experimental results for bubble coalescence obtained by Manga and Stone[13] for determining the functional form of $X_c(B)$.

Figure 2.6 plots the experimental results regarding whether bubbles coalesce with the axes of rescaled initial horizontal separation X_0 and B, where X_0 is defined as:

$$X_0 = x_0^* \mathrm{Bo}^{-2/3} \tag{2.45}$$

X_c is obtained as the boundary between coalescence and no coalescence. This figure also shows the analytical results for $S_{c,\text{asymp}}$ as a black line. It is found that the experimental boundary X_c coincides with the analytical curve $S_{c,\text{asymp}}$ for the entire experimental range of B:

$$X_c \simeq \frac{1}{\sqrt{2}} S_{c,\text{asymp}} \tag{2.46}$$

Thus, the critical horizontal separation x_c^* is approximately equal to the critical vertical separation $s_{c,\text{asymp}}^*$:

$$x_c^* \simeq \frac{1}{\sqrt{2}} s_{c,\text{asymp}}^* \tag{2.47}$$

Note that this relation should be distinguished from $x_c^* \simeq \frac{1}{\sqrt{2}} s_c^*$ because the asymptotic solution is different from the full solution $s_c^* \neq s_{c,\text{asymp}}^*$ for small Bo and λ [Fig. 5(b)]. Using equations (2.44), (2.47) in (2.42), I obtain an analytical expression for the cross-section for coalescence of deformable bubbles, E_deform^* as a function of Bo and λ:

$$E_\text{deform}^*(\mathrm{Bo}, \lambda) = \frac{1}{8} \left(\frac{\sqrt{15}}{2} \frac{(1-\lambda)^{1/2}}{\mathrm{Bo}^{1/2}} + \frac{3}{2}(1-\lambda)^2 \right)^{-2} \tag{2.48}$$

Note that the expression can be simplified in the following two regimes:

$$E_\text{deform}^* \simeq \begin{cases} \dfrac{1}{30} \mathrm{Bo}(1-\lambda)^{-1} & \text{for } \mathrm{Bo} \ll (1-\lambda)^{-3} \quad (2.49) \\ \dfrac{1}{18}(1-\lambda)^{-4} & \text{for } \mathrm{Bo} \gg (1-\lambda)^{-3} \quad (2.50) \end{cases}$$

2.4.2 Unified collision section model

I try to obtain an expression for the cross-section for coalescence of bubbles applicable for the whole Bo range. From the above arguments, I obtain the cross-section for coalescence of deformable bubbles E_deform^* (2.48). Note that our formulation cannot be used for small Bo because I focus on the 'entrain' regime. Actually, the experimental results of Manga and Stone[13] imply that the 'entrain' regime disappears when Bo decreases sufficiently.

To describe the behavior for small Bo, I use the cross-section for coalescence of spherical bubbles E_sphere^* derived in Chapter. 3. I propose a unified expression of the cross-sections for coalescence of spherical and deformable bubbles by

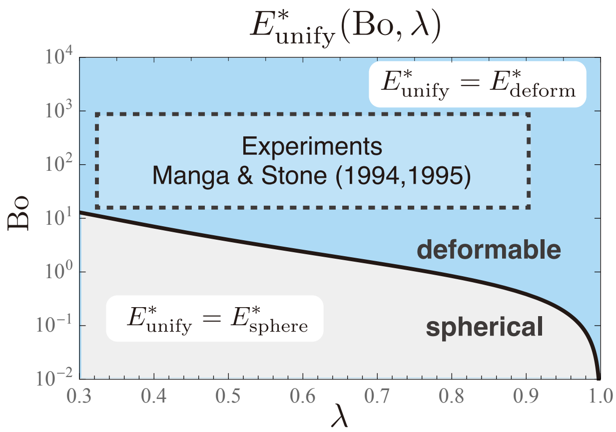

Fig. 2.7: Regime diagram for the unified model of cross-section for coalescence of bubbles. The black line represents the boundary where $E^*_{\rm sphere} = E^*_{\rm deform}$. The gray region represents the region where $E^*_{\rm unify} = E^*_{\rm sphere}$. The blue region represents the region where $E^*_{\rm unify} = E^*_{\rm deform}$. The dashed region represents the experimental parameter range of Manga and Stone[10], [13].

taking the maximum as follows:

$$E^*_{\rm unify}(\mathrm{Bo}, \lambda) = \max\{E^*_{\rm sphere}(\lambda), E^*_{\rm deform}(\mathrm{Bo}, \lambda)\} \tag{2.51}$$

Figure 2.7(c) shows the regime diagram for the unified model. The black line indicates the boundary where $E^*_{\rm sphere} = E^*_{\rm deform}$. The unified expression describes the cross-section for spherical bubbles in the lower grey region and that for deformable bubbles in the upper blue region. Note that the experimental parameters of Manga and Stone (1994) are contained in the large Bo region.

2.4.3 Applications

Manga and Stone[10], [13] provided an empirical model for the cross-section for coalescence of deformable bubbles:

$$E^*_{\rm MS}(\mathrm{Bo}, \lambda) = 0.3\lambda^{1/6} + 0.5\mathrm{Bo}\lambda^6 \tag{2.52}$$

Figure 2.8(a) compares the cross-sections of the theoretical and empirical models with varying Bo for various values of λ. The empirical values are several orders of magnitude larger than the theoretical values for large Bond number $\mathrm{Bo} \gtrsim 10^2$.

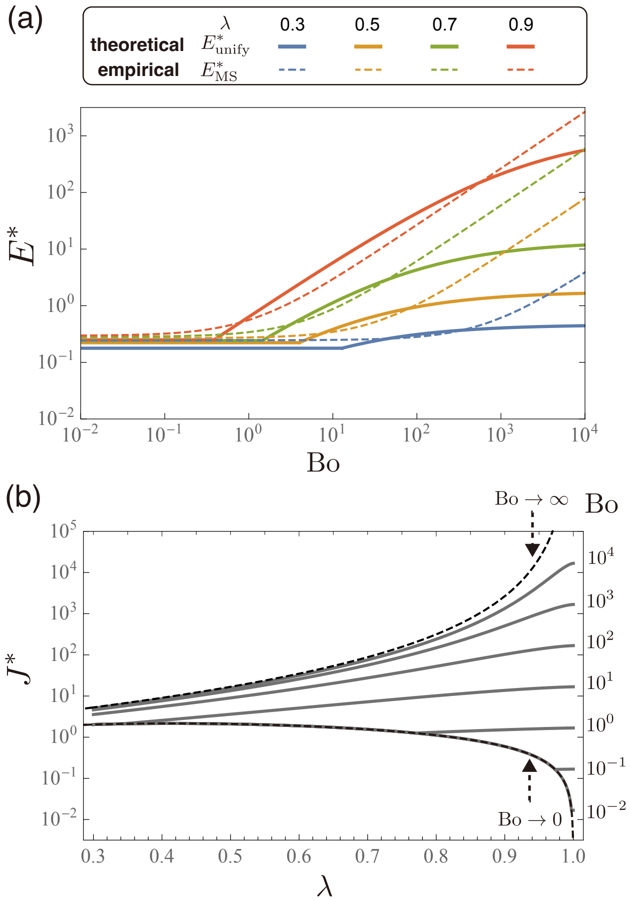

Fig. 2.8: (a) Comparison of the cross-sections for coalescence of bubbles calculated by the theoretical and empirical models. The solid line represents our theoretical model E^*_{unify} (2.51). The dashed line represents the empirical model E^*_{MS} (2.52). The line color represents the size ratio. (b) Normalized coalescence frequency versus size ratio. The solid lines represent theoretical values for the Bond numbers $\mathrm{Bo} = 10^{-2}$ to 10^4. The dashed lines represent the limits for $\mathrm{Bo} \to 0$ (2.56) and for $\mathrm{Bo} \to \infty$ (2.57).

This difference is due to the linear dependence on Bo in the empirical expression, because of the independence of Bo for large Bo in our model as shown by equation (2.50). This independence is reasonable because the bubble motion is dominated by buoyancy force for large Bo, corresponding to low surface tension. Additionally, the experimental data implies independence for $\mathrm{Bo} \approx 100$ (Fig. 2.6). Thus, our theoretical model estimates the cross-section for large Bo more reasonably than the empirical model. Zinchenko et al.[18] numerically calculated the cross-section for $0 < \mathrm{Bo} \leq 20$ by three-dimensional boundary-integral simulations, predicting that the dependence on Bo becomes weak as $\mathrm{Bo} \to 20$ for $\lambda \simeq 1$. Our model is consistent for their predictions and determines the detailed condition of the appearance of Bo independence as a function of λ and Bo, as shown in equations (2.49) and (2.50).

For a dilute suspension, the rate of bubble coalescence is given by the coalescence frequency J as:

$$J = n_1 n_2 \pi x_c^2 (U_{s,2} - U_{s,1}) \tag{2.53}$$

where $n_1,\ n_2$ are the number densities of bubbles having radii of $R_1,\ R_2\ (R_1 < R_2)$. I define the normalized coalescence frequency J^* using the typical length and velocity (2.21) as follows:

$$J^* = \frac{J}{n_1 n_2 \left(\frac{R_1+R_2}{2}\right)^2 U_{s,2}} \tag{2.54}$$

$$= 4\pi(1-\lambda^2)E^*_{\text{unify}} \tag{2.55}$$

Figure 2.8(b) plots the normalized coalescence frequency. From equations (2.50), (2.55), the normalized coalescence frequency increases as Bo increases, and has the following lower and upper limits:

$$J^* \to 4\pi\frac{\lambda(1-\lambda)}{1+\lambda} \quad \text{as} \quad \mathrm{Bo} \to 0 \tag{2.56}$$

$$J^* \to \frac{2\pi}{9}\frac{1+\lambda}{(1-\lambda)^3} \quad \text{as} \quad \mathrm{Bo} \to \infty \tag{2.57}$$

At the limit $\lambda \to 1$, $(1-\lambda)^{-3}$ is infinite, so that the condition for equation (46) is not applicable, because I assume finite Bo. From equations (2.55) and (2.49), the normalized coalescence frequency has the following limit at $\lambda \to 1$:

$$J^* \to \frac{4\pi}{15}\mathrm{Bo} \quad \text{as} \quad \lambda \to 1 \tag{2.58}$$

This result suggests that bubbles with similar sizes frequently coalesce for large Bo in a dilute suspension. Note that the empirical model leads to a coalescence frequency of zero for such bubbles because $E^*_{\mathrm{MS}}(1-\lambda^2) \to 0$ as $\lambda \to 1$.

2.4.4 Limitations

The model of bubble coalescence presented here has the following unsatisfactory points. First, the bubble shape was assumed to be ellipsoidal in the equations for shape evolution (2.4) and viscous mobility (2.7). However, in the experiments, the bubble shapes deviate from ellipsoidal just before they collide (Fig. 2.2). Such bubbles near collision do not change trajectory even if they are greatly distorted. The difference in shapes between our calculations and the experiment only creates a difference in the timescale of the collisions. Thus, the errors may not affect the estimation of the critical separation.

Second, a liquid film formed when the bubbles collide was ignored. The liquid film prevents the coalescence of the bubbles until it ruptures. The time-scale of film drainage depends on the boundary condition of the film interfaces[19]. For mobile interfaces, such as clean liquid without surfactants used by Manga and Stone, the film can be ignored due to its rapid drainage. However, for partially mobile and immobile interfaces, as is sometimes observed in droplet collision for moderate drop-to-medium viscosity ratio[20], the film may not rupture before separation and cannot be ignored. This film condition is out of scope of the present model.

Chapter 3

Theory of Bubble Coalescence in Dilute Suspension

In this chapter, the collision efficiencies of bubbles are theoretically derived by calculating their trajectories. The three driving forces of shear flow and bubble growth as well as buoyancy are considered as factors which drive the relative motion of the bubbles.

3.1 Collision Frequency and Collision Cross Section

Following Manga and Stone (1995), I use a standard model describing particle collisions to calculate the collision-frequency. I consider bubbles in a dilute suspension. I assume that the distribution of bubbles is spatially uniform. I approximate the interaction between two bubbles is dominant and that the third bubble has no contribution. The pair distribution function $p_{ij}(\boldsymbol{r})$ is the probability of finding a size i bubble at a distance between r and $r + dr$ from a size R_j bubble at its center. For a spherical bubble of size R_i, let J_{ij} be the number of times a bubble of size R_j collides with it per unit time. Since two bubbles will collide when they come into close proximity with a relative distance of $r = R_i + R_j$, the collision

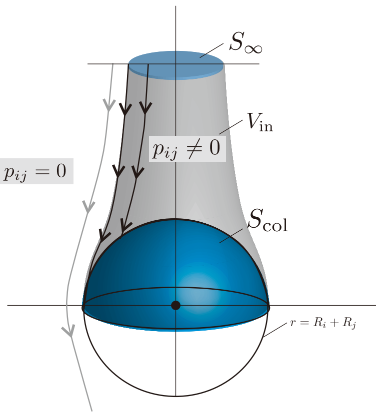

Fig. 3.1: Geometry of relative trajectories.

rate is

$$J_{ij}(t) = -n_i n_j \int_{r=a_i+a_j} p_{ij}(\boldsymbol{r}, t)\boldsymbol{v}_{ij}(\boldsymbol{r}, t) \cdot \boldsymbol{n} dS \tag{3.1}$$

where $\boldsymbol{v}_{ij}$ is the relative velocity between the bubbles.

It is assumed that there is no spatial correlation between bubbles when the distance between bubbles is sufficiently separated.

$$p_{ij}(\boldsymbol{r}) \to 1 \ (\boldsymbol{r} \to \infty) \tag{3.2}$$

Pairs of bubbles that are close enough interact and create spatial correlation. The pair distribution function satisfies the Liouville equation:

$$\frac{\partial p_{ij}}{\partial t} + \nabla \cdot (p_{ij}\boldsymbol{v}_{ij}) = 0 \tag{3.3}$$

If the shape of the bubbles does not change over time and the relative velocity $v_{ij}(\boldsymbol{r})$ between bubbles only depends on the distance r between bubbles, the pair distribution function reaches a steady state. Setting $\frac{\partial p_{12}}{\partial t} = 0$ in Equation (3.3), the expression that the steady-state pair distribution should follow is obtained.

$$\nabla \cdot (p_{ij}\boldsymbol{v}_{ij}) = 0 \tag{3.4}$$

If $\nabla \cdot \boldsymbol{v}_{ij} = 0$, $p_{ij}(\boldsymbol{r})$ can be directly evaluated from Equation (3.4).

$$(\boldsymbol{v}_{ij} \cdot \nabla)\, p_{ij} = 0 \tag{3.5}$$

This means that p_{ij} is constant along the streamlines of v_{ij}. Using the boundary condition (3.2),

$$p_{ij}(\boldsymbol{r}) = 1, \ \boldsymbol{r} \text{ in } V_{\text{in}} \tag{3.6}$$

I derive a useful expression that can be used in the steady state to avoid the explicit evaluation of $p_{12}(\boldsymbol{r})$ near $r = R_1 + R_2$. I define the part of the surface on which $p_{ij} \neq 0$ as S_{col} on the surface $|r| = Ri + Rj$. Equation (3.1) can be rewritten in terms of the surface S_{col} as:

$$J_{ij} = -n_i n_j p_{ij} \int_{S_{\text{col}}} \boldsymbol{v}_{ij} \cdot \boldsymbol{n} dS \tag{3.7}$$

I define the space in which there are streamlines flowing into S_{col} as V_{col}. I define S_∞ as a section of V_{col} far from the origin.

Integrating Equation (3.4) yields

$$\int_{S_0} (p_{ij}\boldsymbol{v}_{ij}) \cdot \boldsymbol{n} dS - \int_{S_\infty} (p_{ij}\boldsymbol{v}_{ij}) \cdot \boldsymbol{n} dS = 0 \tag{3.8}$$

Here, I have used the fact that $\boldsymbol{v}_{12} \cdot \boldsymbol{n} = 0$. Equation (3.1), (3.2), and (3.8) yield the alternative expression

$$J_{ij} = -n_i n_j \int_{S_\infty} \boldsymbol{v}_{ij} \cdot \boldsymbol{n} dS \tag{3.9}$$

If $\boldsymbol{v}_{ij} \to \boldsymbol{v}_{ij}^\infty$ as $|\boldsymbol{r}| \to \infty$ is independennt of position

$$J_{ij} = -n_i n_j \boldsymbol{v}_{ij}^\infty \cdot \int_{S_\infty} \boldsymbol{n} dS \tag{3.10}$$

$$= n_i n_j v_{ij}^\infty S_c \tag{3.11}$$

The collision cross-section S_c is defined as the projection area of S^∞ in the v_{ij}^∞ direction.

3.2 Buoyant Motion

I assume that the bubbles remains spherical shapes at all times. Then the shape tensor is zero at all times.

$$\boldsymbol{A}_i = 0 \tag{3.12}$$

From Equation (2.6), (2.7), and (3.30), the rising velocity of an isolated bubble is given by

$$\boldsymbol{U}_i = U_{s,i}\boldsymbol{e}_z \tag{3.13}$$

where $U_{s,i}$ is the Stokes velocity deifned as:

$$U_{s,i} = \frac{\rho g R_i^2}{3\mu} \tag{3.14}$$

Under assumption (i), $\boldsymbol{u}_j(\boldsymbol{x})$ is the velocity field created by the ascending motion of the spherical bubble j. The velocity field is given as an analytical solution known as Stokeslet:

$$\boldsymbol{u}_j(\boldsymbol{x}) = \frac{R_j U_{s,j}}{2|\boldsymbol{x}-\boldsymbol{x}_j|}\left[\boldsymbol{I} + \frac{(\boldsymbol{x}-\boldsymbol{x}_j)(\boldsymbol{x}-\boldsymbol{x}_j)}{|\boldsymbol{x}-\boldsymbol{x}_j|^2}\right]\boldsymbol{e}_z \tag{3.15}$$

where $\boldsymbol{e}_z$ is a unit vector along the vertical axis z.

Using Equations (2.5), (3.13), and (3.15), I obtain the equation of motion for the two bubbles as follows:

$$\frac{d\boldsymbol{x}_1}{dt} = U_{s,1}\boldsymbol{e}_z + \frac{R_2 U_{s,2}}{2r}\left(\boldsymbol{I} + \frac{\boldsymbol{r}\boldsymbol{r}}{r^2}\right)\boldsymbol{e}_z \tag{3.16}$$

$$\frac{d\boldsymbol{x}_2}{dt} = U_{s,2}\boldsymbol{e}_z + \frac{R_1 U_{s,1}}{2r}\left(\boldsymbol{I} + \frac{\boldsymbol{r}\boldsymbol{r}}{r^2}\right)\boldsymbol{e}_z \tag{3.17}$$

where $\boldsymbol{r}$ is the relative position vector defined as:

$$\boldsymbol{r} = \boldsymbol{x}_1 - \boldsymbol{x}_2 \tag{3.18}$$

Subtracting Equation (3.17) from Equation (3.16), I obtain the relative velocity between the bubbles:

$$\boldsymbol{v}_{12}(\boldsymbol{r}) = (U_{s,1} - U_{s,2})\,\boldsymbol{e}_z - \frac{R_1 U_{s,1} - R_2 U_{s,2}}{2r}\left(\boldsymbol{I} + \frac{\boldsymbol{r}\boldsymbol{r}}{r^2}\right)\boldsymbol{e}_z \tag{3.19}$$

This equation is written in polar coordinate (r, θ) as follows:

$$\frac{dr}{dt} = -\left(U_{s,1} - U_{s,2}\right)\cos\theta + \frac{R_1 U_{s,1} - R_2 U_{s,2}}{r}\cos\theta \tag{3.20}$$

$$r\frac{d\theta}{dt} = \left(U_{s,1} - U_{s,2}\right)\sin\theta - \frac{R_1 U_{s,1} - R_2 U_{s,2}}{2r}\sin\theta \tag{3.21}$$

Removing t from Equations (3.20) and (3.21), I obtain the trajectory equation:

$$\frac{1}{r}\frac{dr}{d\theta} = -\frac{(U_{s,1} - U_{s,2}) - (R_1 U_{s,1} - R_2 U_{s,2})\frac{1}{r}}{(U_{s,1} - U_{s,2}) - (R_1 U_{s,1} - R_2 U_{s,2})\frac{1}{2r}} \cdot \frac{\cos\theta}{\sin\theta} \tag{3.22}$$

Separating and integrating Equation (3.22) with an initial condition $r = r_0 \gg 1$ and $\theta = \theta_0$, I obtain the

$$\frac{r - \frac{R_1 U_1 - R_2 U_2}{U_1 - U_2}}{r_0} = \frac{r_0 \sin\theta_0}{r \sin\theta} \tag{3.23}$$

$r = R_1 + R_2, \theta = \pi/2$. $x_c = r_0 \sin\theta_0$.

$$x_c^2 = R_1 R_2 \tag{3.24}$$

The collision efficiency is defined as the collisional cross-section ratio to geometric cross-section

$$E = \frac{R_1 R_2}{(R_1 + R_2)^2} \tag{3.25}$$

$$= \frac{\lambda}{(1+\lambda)^2} \tag{3.26}$$

The collision efficiency is a function of size ratio $\lambda = \frac{R_2}{R_1}$. This analytical expression is consistent with the exact solution given by Zinchenko[21] (Fig. 3.2).

The collision frequency function without hydrodynamic interaction is explicitly written as:

$$J_{12} = \pi(R_1 + R_2)^2 |U_1 - U_2| \tag{3.27}$$

The collision frequency function with hydrodynamic interaction is explicitly written as:

$$J_{12} = \pi R_1 R_2 |U_1 - U_2| \tag{3.28}$$

3.3 Shear Flow

I assume that the bubbles remains spherical shapes at all times. Then the shape tensor is zero at all times.

$$\boldsymbol{A}_i = 0 \tag{3.29}$$

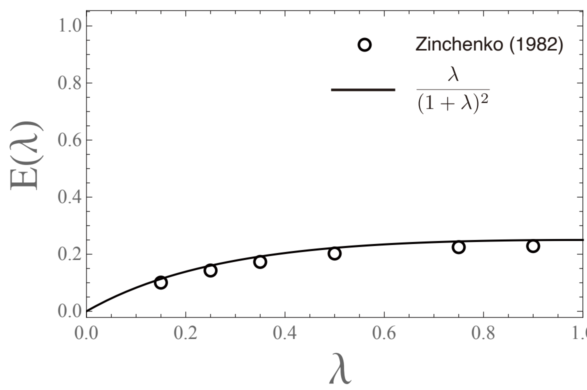

Fig. 3.2: Collision efficiency for two spherical bubbles in gravity field as a function of size ratio λ. The black line is obtained from the exact solution, Zinchenko (1982)[21]. The black line is obtained from the first order approxiamtion.

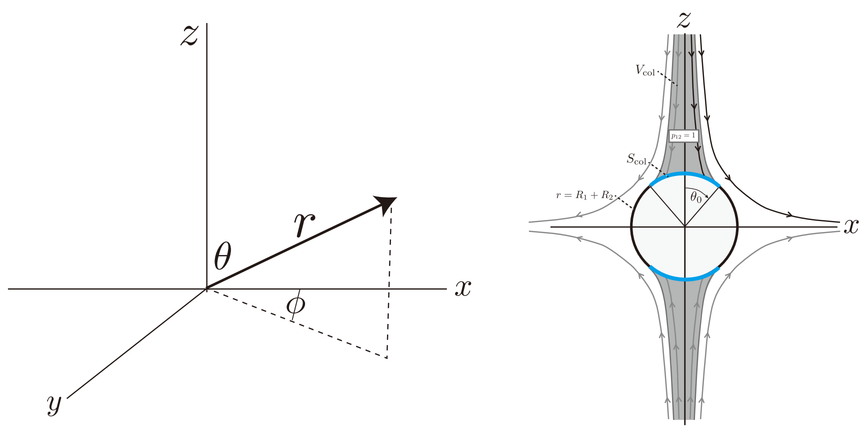

Fig. 3.3: Geometry of the relative trajectory for shear motion.

The buoyant forces acting on the bubbles are neglected.

$$\boldsymbol{F}_i = 0 \tag{3.30}$$

An isolated bubble in a shear flow creates a velocity field around it. The velocity field is given as an analytical solution known as Stresslet:

$$\boldsymbol{u}_i(\boldsymbol{x}) = \frac{R_i^3}{|\boldsymbol{x}-\boldsymbol{x}_i|^3}\boldsymbol{E}^\infty(\boldsymbol{x}-\boldsymbol{x}_i)\cdot\frac{(\boldsymbol{x}-\boldsymbol{x}_i)(\boldsymbol{x}-\boldsymbol{x}_i)}{|\boldsymbol{x}-\boldsymbol{x}_i|^2} \tag{3.31}$$

The rigid-rotation of the ambient flow $\boldsymbol{\Omega}^\infty$ has no contribution to the velocity field. Using Equations (2.5) and (3.31), I obtain the equation of motion for the two bubbles in a linear flow as follows:

$$\frac{d\boldsymbol{x}_1}{dt} = \boldsymbol{\Omega}^\infty \times \boldsymbol{x}_1 + \boldsymbol{E}^\infty\boldsymbol{x}_1 - \frac{R_2^3}{r^3}(\boldsymbol{E}^\infty\boldsymbol{r})\cdot\frac{\boldsymbol{r}\boldsymbol{r}}{r^2} \tag{3.32}$$

$$\frac{d\boldsymbol{x}_2}{dt} = \boldsymbol{\Omega}^\infty \times \boldsymbol{x}_2 + \boldsymbol{E}^\infty\boldsymbol{x}_2 + \frac{R_1^3}{r^3}(\boldsymbol{E}^\infty\boldsymbol{r})\cdot\frac{\boldsymbol{r}\boldsymbol{r}}{r^2} \tag{3.33}$$

Subtracting Equation (3.33) from Equation (3.32), I obtain the relative velocity between the bubbles.

$$\boldsymbol{v}_{12}(\boldsymbol{r}) = \boldsymbol{\Omega}^\infty \times \boldsymbol{r} + \boldsymbol{E}^\infty\boldsymbol{r} - A(r)(\boldsymbol{E}^\infty\boldsymbol{r})\cdot\frac{\boldsymbol{r}\boldsymbol{r}}{r^2} \tag{3.34}$$

where $A(r)$ is the mobillity function corresponding to the hydrodynamic interaction defined as:

$$A(r) = \frac{R_1^3 + R_2^3}{r^3} \tag{3.35}$$

The divergence of the relative velocity is zero as follows:

$$\nabla\cdot\boldsymbol{v}_{12} = \nabla\cdot(\boldsymbol{\Omega}^\infty\times\boldsymbol{r} + \boldsymbol{E}^\infty\boldsymbol{r}) - \nabla\cdot\left[A(r)(\boldsymbol{E}^\infty\boldsymbol{r})\cdot\frac{\boldsymbol{r}\boldsymbol{r}}{r^2}\right] \tag{3.36}$$

$$= -\left[3A(r) + r\frac{dA(r)}{dr}\right]\boldsymbol{r}\cdot(\boldsymbol{r}\boldsymbol{E}^\infty) \tag{3.37}$$

$$= 0 \tag{3.38}$$

where the last equality follows from Equation (3.35).

First, I consider a pure shear flow subjected to the bubbles.

$$\boldsymbol{u}^\infty(\boldsymbol{x}) = (-\dot{\gamma}x, -\dot{\gamma}y, 2\dot{\gamma}z) \tag{3.39}$$

where $\dot{\gamma}$ is the strain rate. Then the strain tensor and rigid rotation of the flow is given as follows:

$$\boldsymbol{E}^{\infty} = \begin{bmatrix} -\dot{\gamma} & 0 & 0 \\ 0 & -\dot{\gamma} & 0 \\ 0 & 0 & 2\dot{\gamma} \end{bmatrix} \tag{3.40}$$

$$\boldsymbol{\Omega}^{\infty} = \begin{bmatrix} 0 \\ 0 \\ 0 \end{bmatrix} \tag{3.41}$$

Using Equations (3.39), (3.40), and (3.41), the relative velocity in spherical coordinate (r, θ, ϕ) is given as follows:

$$v_{12,r} = -r\dot{\gamma}\,(1 - A(r))\left(3\cos^2\theta - 1\right) \tag{3.42}$$

$$v_{12,\theta} = 3r\dot{\gamma}\sin\theta\cos\theta \tag{3.43}$$

$$v_{12,\phi} = 0 \tag{3.44}$$

To evalute the collision rate, I study the trajectory of the marker particle moving with relative velocity $\boldsymbol{v}_{12}(\boldsymbol{r})$. Equation (3.42) and (3.42) yields the trajectory equation for the position of the marker particle position $r = r(\theta)$.

$$\frac{dr}{d\theta} = -r\,(1 - A(r))\,\frac{3\cos^2\theta - 1}{3\sin\theta\cos\theta} \tag{3.45}$$

Fig. 3.3 shows the trajectory of the particle originating at a point far from the origin. The shaded area represents the region at which the particle comes into the surface $r = R_1 + R_2$. The blue area represents the region on the surface $r = R_1 + R_2$.. The critical angle θ_0 satisfies $\cos\theta_0 = \frac{1}{\sqrt{3}}$ corresponding to $\frac{dr}{d\theta}(\theta_0) = 0$. As I discuss in Section 3.1, $p_{12}(\boldsymbol{r}) = 1$ on S_{col} due to the zero divergence of the relative velocity (3.38). Using Equation (3.42) and (3.7), I obtain the collision rate for the bubbles in pure shear:

$$J_{12} = \frac{8\pi}{3\sqrt{3}} n_1 n_2 \dot{\gamma} (R_1 + R_2)^3 E_{\text{axisym}} \tag{3.46}$$

where E_{pure} is the collision efficinecy for pure shear defined as

$$E_{\text{pure}} = 1 - A(R_1 + R_2) \tag{3.47}$$

$$= \frac{3R_1R_2}{(R_1 + R_2)^2} \tag{3.48}$$

where the last equality follows from Equation (3.35).

Second, I consider a simple shear flow subjected to the bubbles.

$$\boldsymbol{u}^{\infty} = (\dot{\gamma} y, 0, 0) \tag{3.49}$$

Then the strain tensor and rigid rotation of the flow is given as follows:

$$\boldsymbol{E}^{\infty} = \begin{bmatrix} 0 & \frac{1}{2}\dot{\gamma} & 0 \\ \frac{1}{2}\dot{\gamma} & 0 & 0 \\ 0 & 0 & 0 \end{bmatrix} \tag{3.50}$$

$$\boldsymbol{\Omega}^{\infty} = \begin{bmatrix} 0 \\ 0 \\ -\frac{1}{2}\dot{\gamma} \end{bmatrix} \tag{3.51}$$

Then the equation of relative motion is written in spherical coordinate as follows:

$$v_{12,r} = r\dot{\gamma}\left(1 - A(r)\right)\sin^2\theta \sin\phi \cos\phi \tag{3.52}$$

$$v_{12,\theta} = -r\dot{\gamma}\sin^2\phi \tag{3.53}$$

$$v_{12,\phi} = r\dot{\gamma}\sin^2\theta \cos\theta \sin\phi \cos\phi \tag{3.54}$$

Similarly, using Equation (3.7), (3.52), (3.53), and (3.54), I obtain the collision rate for the bubbles in simple shear:

$$J_{12} = \frac{4}{3} n_1 n_2 \dot{\gamma} (R_1 + R_2)^3 E_{\text{simple}} \tag{3.55}$$

where E_{simple} is the collision efficinecy for simple shear.

Similarly, the collision eficiency is theoretically derived as:

$$E_{\text{simple}} = \frac{3R_1 R_2}{(R_1 + R_2)^2} \tag{3.56}$$

3.4 Bubble Growth

Extending the theory of collision rate for growing droplets[22][23], I drive the collision rate of growing bubbles. An isolated growing bubble creates an extensional flow that is spherical symmetrical around the bubble. The velocity of the created flow is determined by the equation of continuity:

$$\frac{1}{r^2}\frac{\partial}{\partial r}\left(r^2 u\right) = 0 \tag{3.57}$$

where r is the radial distasnce from the bubble center and u is the radial velocity of the created flow. Integrating Equation (3.57) from the bubble surface at $r = R_i$ to a certain point yields:

$$u_i(r,t) = \frac{R_i(t)^2}{r^2}\dot{R}_i(t) \tag{3.58}$$

where $R_i(t)$ is the bubble radius as a function of time. Equation (3.58) yields the relative velocity between bubble R_1 and bubble R_2.

$$\boldsymbol{u}_{12}(\boldsymbol{r},t) = \left[\frac{R_1(t)^2}{r^2}\dot{R}_1(t) + \frac{R_2(t)^2}{r^2}\dot{R}_2(t)\right]\frac{\boldsymbol{r}}{r} \tag{3.59}$$

$$= \frac{1}{r^2}\left(R_1^2\dot{R}_1 + R_2^2\dot{R}_2\right)\frac{\boldsymbol{r}}{r} \tag{3.60}$$

where r is the distance between the bubbles. The collision rate for growing bubbles is given by modifying the relative velocity in Equation (3.1) as follows:

$$J_{12}(t) = -n_1 n_2 \int_{r=R_1+R_2} p_{12}(\boldsymbol{r},t)\left[\boldsymbol{u}_{12}(\boldsymbol{r},t) - \boldsymbol{u}^S(\boldsymbol{r},t)\right]\cdot \boldsymbol{n} dS \tag{3.61}$$

where $\boldsymbol{u}^S(t)$ is the total velocity of the bubble surfaces:

$$\boldsymbol{u}^S(\boldsymbol{r},t) = \left(\dot{R}_1 + \dot{R}_2\right)\frac{\boldsymbol{r}}{r} \tag{3.62}$$

The pair-distribution function is spherical symmetric due to spherical symmetricity of the relative velocity (3.60). This reduces the collision rate to the following form:

$$J_{12}(t) = -4\pi n_1 n_2 (R_1+R_2)^2 p_{12}(R_1+R_2,t)\left[u_{12}(R_1+R_2,t) - u^S(t)\right] \tag{3.63}$$

Solving Equation (3.3) and finding $p_{12}(\boldsymbol{r},t)$ is useful way to calculate J_{12}. Equation (3.3), (3.60) yield:

$$\frac{\partial p_{12}}{\partial t} + \frac{\partial}{\partial r}(u_{12}p_{12}) = 0 \tag{3.64}$$

The initial and boundary conditions for the pair-distribution function is:

$$p_{12}(r,0) = 1 \tag{3.65}$$

$$p_{12}(r,t) \to 1 \text{ as } r \to \infty \tag{3.66}$$

Without hydrodynamic interaction $u_{12} = 0$, p_{12} is steady and uniform. Equation (3.62, (3.64) and (3.65) yield:

$$p_{12}(r,t) = p_{12}(r,0) \tag{3.67}$$
$$= 1 \tag{3.68}$$

Equation (3.68), (3.63), and $u_{12} = 0$ yield the formula of the collision rate for growing bubbles without hydrodynamic interaction.

$$J_{12}^{(0)}(t) = 4\pi n_1 n_2 (R_1 + R_2)^2 (\dot{R}_1 + \dot{R}_2) \tag{3.69}$$

Thus, I obtain the collision efficiency as follows:

$$E = 1 - \frac{\dot{v}_1 + \dot{v}_2}{(v_1^{1/3} + v_2^{1/3})^2 (v_1^{-2/3+\omega} + v_2^{-2/3+\omega})} \tag{3.70}$$

See Appendix. A.2 for the derivation of the non-steady case.

Chapter 4

Evolution of uniform bubble suspension

The goal of this chapter is to clarify the relationship between the newly derived microscopic coalescence frequency function (presented in Chapter 3) and the macroscopic evolution of size distributions. I perform numerical simulations of the evolution of BSD and derive useful empirical formulas for the evolution of BSD under simplified conditions. I consider the four conditions of the bubble coalescence driven by buoyancy, shear flow, diffusion-limited growth, viscosity-limited growth, and isothermal expansion. As a result, I find that, for coalescence driven by buoyancy, shear flow, viscosty-limited growth, and isothermal expansion, the bubbles rapidly coalesce and their size distribution shows power-law with a slope of -2. I also find that, for coalescence driven by diffusion-limited growth, the bubbles orderly coalesce and the size distribution shows power-law with a slope of -0.5.

4.1 Formulation

4.1.1 Bubble coalescence equation

I follow the standard formulation of the particle coagulation problem governed by the Smoluchowski coagulation equation [9]. I consider a dilute suspension of bubbles that are uniformly distributed in space. The suspension of bubbles is characterized by the bubble size distribution function $n(v,t)$. $n(v,t)dv$ represents the number of bubbles per unit volume in the range of volume from v to $v+dv$ at time t. The dimension of $n(v,t)$ is $[1/L^6]$.

Bubbles with volumes v and v' collide at a rate $J(v,v')$ and coalesce into a larger bubble with volume $v+v'$, where $J(v,v')$ is a collision frequency function (presented in Chapter. 3). The change in the number of bubbles with volume v is thus given as follows:

$$J(v,v',t) = n(v,t)n(v',t)K(v,v') \tag{4.1}$$

$$\Omega(v,[n]) = \frac{1}{2}\int_0^v n(v-v')n(v')K(v-v',v')dV' - n(v)\int_0^\infty n(v')K(v,v')dV' \tag{4.2}$$

The first term on the right-hand side represents gain from the coalescence of bubbles with volumes v' and $v-v'$ smaller than volume v. The seond term represents loss from the coalescence of bubbles with volumes v and v'. Ω is a functional of the size distribution function $n(v,t)$. I only consider two-body collision due to the diluteness of the bubbles, and assume that two collided bubbles always coalesce by rupturing film between them.

I consider that a bubble with volume v grows at a growth rate $\Gamma(v,t)$. The growth rate is assumed to the following algebric form:

$$\Gamma(v) = av^\omega \tag{4.3}$$

where the constants a and ω depend on the mechanism of bubble growth.

Equation (4.2) and (4.3) yields the equation for the evolution of the bubble size distribution as follows:

$$\frac{\partial n}{\partial t}(v,t) + \frac{\partial}{\partial v}\left(\Gamma(v,t)n\right) = \Omega_{col}(v,[n]) \tag{4.4}$$

I assume that bubble volumes are initially distributed around v_0 with a width ΔV_0, whose volume fraction in suspension is ϕ_0. The initial bubble size distribution is given as follows:

$$n(v,0) = \frac{\phi_0}{v\Delta v_0}\Theta_{v_0,\Delta v}(v) \tag{4.5}$$

where $\Theta_{v_0,\Delta v_0}(v)$ is a function that returns unity for v within $[a^{-1}v_0, av_0]$ and zero otherwise. The constant a is chosen such that the initial distribution has the given volume fraction:

$$\int_0^\infty n(v,0)vdv = \phi_0 \tag{4.6}$$

In this study, the initial width is fixed at $\Delta v_0 = 0.1v_0$.

4.1.2 Non-dimensionalization

Non-dimensional variables are introduced as follows:

$$n = \frac{\phi_0}{v_0^2}n^* \tag{4.7}$$

$$v = v_0 v^* \tag{4.8}$$

$$t = \tau t^* \tag{4.9}$$

$$K(v,v') = \frac{v_0}{\tau}K^*(v^*, v'*) \tag{4.10}$$

$$\Omega(v,[n]) = \frac{\phi_0 v_0}{\tau}\Omega^*(v^*,[n^*]) \tag{4.11}$$

$$\begin{aligned}\Omega^*(v^*,[n^*]) = \frac{1}{2}\int_0^{v^*} & k(v^*,v'*)n(v^*-v^{'*},t^*)n(v^{'*},t^*) \\ - n(v^{'*},t^*) & \int_0^\infty k(v^*,v'*)n(v^*-v^{'*},t^*)\end{aligned} \tag{4.12}$$

The explicit form of the non-dimensionalized coalescence equation is given later.

4.1.3 Momentum equations

The i-th order moment of the bubble size distribution is defined as:

$$\mathcal{M}_i = \int_0^\infty n(v,t)v^i dv \tag{4.13}$$

The non-dimensinoal form is given as follows:

$$\mathcal{M}_i^* = \int_0^\infty dv^* v^{*i} n^*(v^*, t^*) \tag{4.14}$$

$$\mathcal{M}_i = \phi_0 v_0^{i-1} \mathcal{M}_i^* \tag{4.15}$$

I define the bubble number density N and the vesicularity ϕ as the zeroth and first order moments of the bubble size distribution, respectively:

$$\begin{aligned} N(t) &= \mathcal{M}_0 \\ \phi(t) &= \mathcal{M}_1 \end{aligned} \tag{4.16}$$

Integrating Equation (4.4) yields the equation of motion for the moments:

$$\frac{dN}{dt} = -\frac{1}{2} \int_0^\infty \int_0^\infty J(v, v') n(v, t) n'(v', t) dv dv' \tag{4.17}$$

$$\frac{d\phi}{dt} = \int_0^\infty \Gamma(v, t) n(v, t) dv \tag{4.18}$$

If I assume $\Gamma(v, t) = a v^\omega$,

$$\frac{d\phi}{dt} = a M_\omega(t) \tag{4.19}$$

4.2 Numerical Methods

I describe the numerical method to solve the equation of bubble coalescence and growth (4.4). The volume space is discretized into logarithmically-spaced N bins.

$$v_k = 10^{k/N_{bd}} v_{k-1} \; k = 1 \ldots N \tag{4.20}$$

where N_{bd} is the number of bins per decade. I take N_{bd} from 15 to 40 depending on the detail of problems.

I use the following variable V instead of the number density n.

$$V_k = \int_{v_{k-1/2}}^{v_{k+1/2}} n(v, t) v dv \tag{4.21}$$

This ensures the conservation of the total volume defined as $\sum_{k=1}^N V_k$.

I solve the coalescence equation with a fractional step method, treating separately the coalescece term and the growth term as the following two equations.

$$\frac{\partial n}{\partial t} = \Omega(v, [n]) \tag{4.22}$$
$$\frac{\partial n}{\partial t} = -\frac{\partial}{\partial v}(\Gamma(v)n(v,t)) \tag{4.23}$$

I take the following two steps to update the variable V_k^n at time t_n to the distribution V_k^{n+1} at time $t_{n+1} = t_n + \Delta t$. First, the contribuion of the bubble coalescence is calculated from Equation (4.22).

$$\bar{V}_k^n = V_k^n + \Delta t A_k^n \tag{4.24}$$

where A_k^n is equivalant to the right hand-side of Equation (4.22), which is calculated from V_k^n using the method of Lee (2000)[24]. Next, the contribuion of the bubble growth is calculated from Equation (4.23).

$$V_k^{n+1} = \bar{V}_k^n + \Delta t B_k^n \tag{4.25}$$

where B_k^n is equivalant to the right hand-side of Equation (4.23), which is calculated from $\bar{V}_k^n$ using the RCIP method[25][26].

4.3 Numerical Results

I conducted numerical calculations to examine four cases with different modes of coalescence and growth. First, neglecting bubble growth, I studied coalescence driven by buoyancy in Section 4.3.1 and shear in Section 4.3.2. Next, I formulate bubble coalescecne with growth in Section 4.3.3, and, then considering only bubble growth, I studied coalescence driven by diffusion-limited growth in Section 4.3.4 and viscosity-limited growth in Section 4.3.5. Finally, I determined the scaling functions of the distributions in Section 4.3.7.

4.3.1 Ascending motion

The collision frequency function for ascending bubbles is given by:

$$K_{\text{buo}}(v_1, v_2) = \pi R_1 R_2 \left| U_1 - U_2 \right| \tag{4.26}$$

where U and U' are terminal velocities of bubbles in a surrounding viscous liquid, defined as:

$$U_i = \frac{\rho g R_i^2}{3\mu} \tag{4.27}$$

where ρ is the fluid density, g is the acceleration due to gravity, R_i is the radius of the bubble, and μ is the fluid viscosity. Here, I define an equivalant radius as:

$$v_i = \frac{4\pi}{3} R_i^3 \tag{4.28}$$

Bubble growth is neglected for simplicity.

$$\Gamma = 0 \tag{4.29}$$

The time scale for non-dimensionalization is chosen as

$$\tau_{buo} = \frac{3\mu}{\rho g R_0} \tag{4.30}$$

As a result, I obtain the non-dimesnionalized equation for the evolution of BSD as follows:

$$\begin{aligned} \frac{1}{\phi_0}\frac{\partial n^*(v^*,t^*)}{\partial t^*} &= \frac{1}{2}\int_0^{v^*} K^*_{\mathrm{buo}}(v^* - v^{'*}, v'*) n^*(v^* - v^{'*}, t^*) n^*(v^{'*}, t^*) dv^{'*} \\ &- n^*(v^*,t^*) \int_0^\infty K^*_{\mathrm{buo}}(v^*, v'*) n^*(v^{'*}, t^*) dv^{'*} \end{aligned} \tag{4.31}$$

This resulting equation contains no parameters with the scaled time variable $\phi_0 t^*$. The non-dimensionalized coalescence kernel is given by

$$K^*_{\mathrm{buo}}(v_1^*, v_2^*) = (v_1^* v_2^*)^{1/3} \left| v_1^{*1/3} - v_2^{*1/3} \right| \tag{4.32}$$

Fig. 4.1 shows the evolution of the size distribution. As time passes, the small size parts of the initial distribution remain the same, while the large size parts extend to the right, forming the power-law:

$$n^* \propto v^{*-2.01} \tag{4.33}$$

The leading edge of the distribution rapidly diverges at $\phi_0 t^* \approx 10^{0.6}$. The critical time of divergence is defined as t_c.

$$t_c^* = 4.72\phi_0^{-1} \tag{4.34}$$

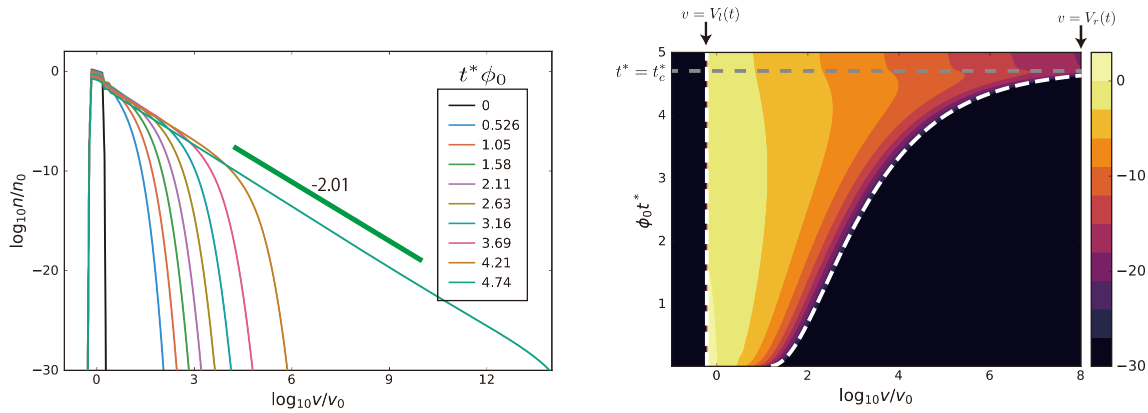

Fig. 4.1: Evolution of the bubble size distribution due to coalescence driven by buoyancy. (a) The size distribution is plotted against volume and number. The green bold line represents the slope of the power-law $n \propto v^{-2.01}$, and the other lines represent the distribution profiles at different times, as indicated in the legend box. (b) The size distribution is plotted against volume and time, with color intensity representing number. The number is normalized by the initial number n_0, the volume is normalized by the initial volume v_0, and the time is scaled by the initial volume fraction ϕ_0. The white dashed lines represent the minimum volume V_l and the maximum volume V_r, and the gray dashed line indicates the critical time $t = t_c$. Both horizontal and vertical axes are displayed on a logarithmic scale.

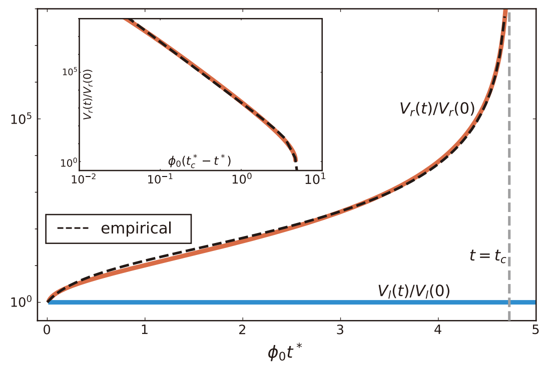

Fig. 4.2: Evolution of the minimum and maximum volumes of the size distribution due to coalescence driven by buoyancy. The blue line represents the minimum volume, $V_l(t)$, and the orange line represents the maximum volume, $V_r(t)$, both normalized by their respective initial values $V_l(0)$ and $V_r(0)$. The time axis is scaled by the initial volume fraction ϕ_0. The gray dashed line indicates the critical time $t = t_c$. The orange dashed line represents the empirical curve of the maximum volume, given by Equation (4.36). The inset plot focuses on the evolution of the maximum volume near the critical time. Both the horizontal and vertical axes are displayed on a logarithmic scale.

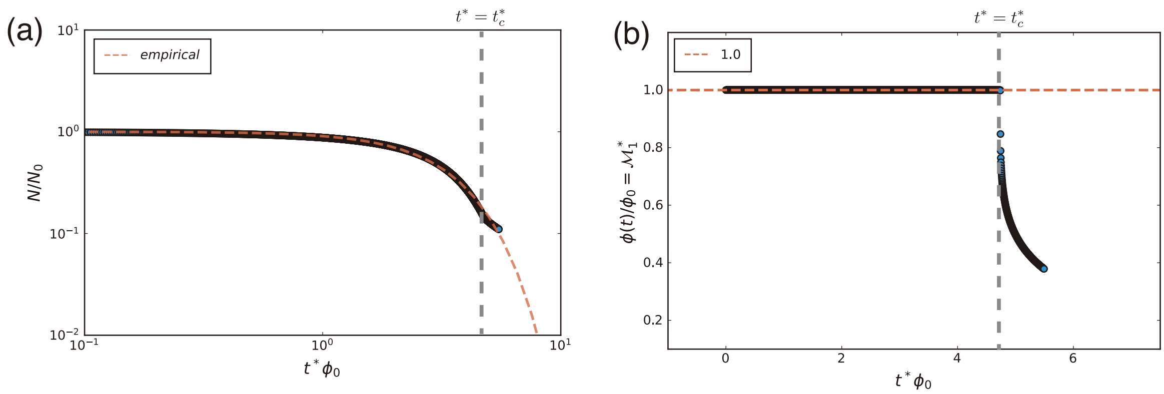

Fig. 4.3: Evolution of the moments of the bubble size distribution in coalescence driven by buoyancy. (a) Evolution of bubble number density, represented by the blue line. The time axis is scaled by the initial volume fraction ϕ_0. The gray dashed line indicates the critical time $t = t_c$. The orange line shows the empirical curve of the maximum volume, calculated using Equation (4.38). (b) Evolution of bubble volume fraction, represented by the blue line. The orange dashed line represents a value of 1.0. Both the horizontal and vertical axes use logarithmic scales.

The white line in Fig. 4.1b is a contour where $n(v,t) = n_0 10^{-20}$. The left and right white lines are defined as $V_l(t)$ and $V_r(t)$, respectively. Fig. 4.2 shows the detailed evolution of $V_l(t)$ and $V_r(t)$. V_l takes a constant value, while V_r diverges at $t = t_c$ as the following empriical formulas:

$$V_l(t)/V_l(0) = 1 \tag{4.35}$$

$$\begin{aligned} V_r(t)/V_r(0) &= 1 + 10^{3.7}\left\{\phi_0^{-3.4}(t_c^* - t^*)^{-3.4} - 4.73^{-3.4}\right\} && (4.36)\\ &\approx 10^{3.7}\phi_0^{-3.4}(t_c^* - t^*)^{-3.4} \quad \text{for} \quad t^* \approx t_c^* && (4.37) \end{aligned}$$

Fig. 4.3 shows the evolution of the moments of BSD. The number density of bubbles decreases exponentially and shows no singular behavior near $t = t_c$ as the following empirical formula:

$$N(t)/N(0) = \exp\left(-0.1(t^*\phi_0)^{1.85}\right) \tag{4.38}$$

The volume fraction of the bubbles remains constant because bubble growth is neglected.

$$\phi(t)/\phi(0) = 1 \tag{4.39}$$

The volume fraction decreases after $t > t_c$ due to the removal of the maximum bubble size volume.

4.3.2 Shear motion

The collision frequency function for bubbles under shear deformation is given by:

$$K_{\text{shear}}(v_1, v_2) = C_{\text{shear}} R_1 R_2 (R_1 + R_2)^2 \dot{\gamma} \tag{4.40}$$

where $\dot{\gamma}$ is strain rate and C_{shear} is a constant defined as:

$$C = \begin{cases} \frac{8}{\sqrt{3}} \approx 4.6 & \text{pure shear} \\ 4 & \text{simple shear} \end{cases} \tag{4.41}$$

Similarly to the ascending motion in Section 4.3.1, the growth of the bubbles is neglected.

$$\Gamma = 0 \tag{4.42}$$

The time scale for non-dimensionalization is chosen as

$$\tau_{\text{shear}} = \dot{\gamma}^{-1} \tag{4.43}$$

As a result, I obtain the non-dimesnionalized equation for the evolution of BSD as follows:

$$\begin{aligned}\frac{1}{\phi_0}\frac{\partial n^*(v^*,t^*)}{\partial t^*} = \frac{1}{2}\int_0^{v^*} & K^*_{\text{shear}}(v^*-v^{'*}, v'*)n^*(v^*-v^{'*},t^*)n^*(v^{'*},t^*)dv^{'*} \\ &- n^*(v^*,t^*)\int_0^{\infty} K^*_{\text{shear}}(v^*, v'*)n^*(v^{'*},t^*)dv^{'*} \end{aligned} \tag{4.44}$$

This resulting equation contains no parameters with the scaled time variable $\phi_0 t^*$.

$$K^*_{\text{shear}}(v_1^*, v_2^*) = (v_1^* v_2^*)^{1/3}\left(v_1^{*1/3} + v_2^{*1/3}\right)^2 \tag{4.45}$$

Fig. 4.4 shows the evolution of BSD. As time progresses, the initial distribution remains the same, while the right end of the distribution shifts to the right, eventually diverging in an exponential manner. The distribution takes on a power-law form with a slope of -2. The evolution of characteristic volumes V_l and V_r are also plotted. V_r moves along the right end of the distribution in an exponential manner.

$$V_l(t)/V_l(0) = 1 \tag{4.46}$$

$$V_r(t)/V_r(0) = e^{2.0(t^*\phi_0)^{0.82}} \tag{4.47}$$

Fig. 4.6 shows the evolution of moments. The number density first decreases exponentially, then decreases in proportion to $(t^*\phi_0)^{-1}$ for $t^*\phi_0 > 10$. An empirical formula was derived from this.

$$\begin{aligned} N(t)/N(0) &= \frac{1}{2}\left(e^{-0.8\phi_0 t^*} + \frac{1}{1+2\phi_0 t^*}\right) \qquad (4.48)\\ &\approx 0.25(\phi_0 t^*)^{-1} \text{ for } t \gg \phi_0^{-1} \qquad (4.49)\end{aligned}$$

The volume fraction of foaming remains constant until V_2 reaches $V_{\max}$, becauses the growth of the bubbles is neglected

$$\phi(t)/\phi_0 = 1 \tag{4.50}$$

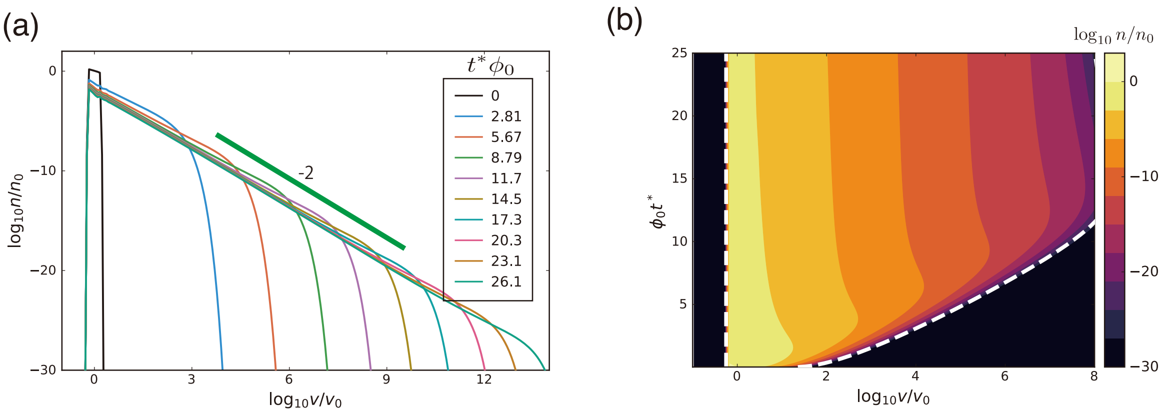

Fig. 4.4: Evolution of the bubble size distribution due to coalescence driven by shear. (a) The size distribution is plotted against volume and number. The green bold line represents the slope of the power-law $n \propto v^{-2}$, and the other lines represent the distribution profiles at different times, as indicated in the legend box. (b) The size distribution is plotted against volume and time, with color intensity representing number. The number is normalized by the initial number n_0, the volume is normalized by the initial volume v_0, and the time is scaled by the initial volume fraction ϕ_0. The white dashed lines represent the minimum volume V_l and the maximum volume V_r. Both horizontal and vertical axes are displayed on a logarithmic scale.

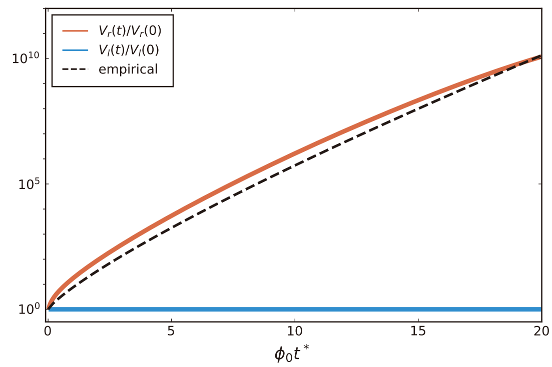

Fig. 4.5: Evolution of the minimum and maximum volumes of the size distribution due to coalescence driven by shear. The blue line represents the minimum volume, $V_l(t)$, and the orange line represents the maximum volume, $V_r(t)$, both normalized by their respective initial values $V_l(0)$ and $V_r(0)$. The time axis is scaled by the initial volume fraction ϕ_0. The dashed line represents the empirical curve given by Equation (4.47). Both the horizontal and vertical axes are displayed on a logarithmic scale.

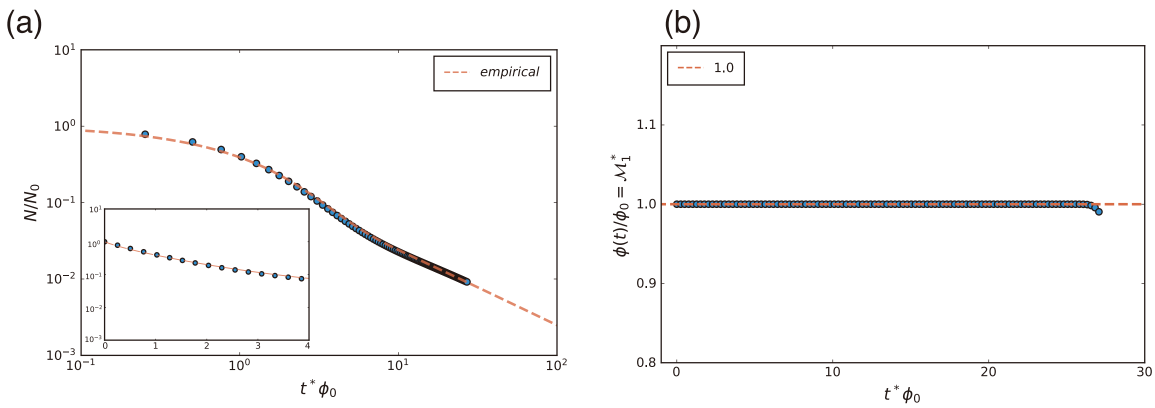

Fig. 4.6: Evolution of the moments of the bubble size distribution in coalescence driven by shear. (a) Evolution of bubble number density, represented by the blue markers. The time axis is scaled by the initial volume fraction ϕ_0. The dashed line shows the empirical curve given by Equation (4.38). THe inset plot focuses on the evolution near the initial time. (b) Evolution of bubble volume fraction, represented by the blue line. The orange dashed line represents a value of 1.0. Both the horizontal and vertical axes use logarithmic scales.

4.3.3 Bubble growth under step decompression

The collision frequency function for growing bubbles is given by:

$$K_{\text{growth}}(v_1, v_2) = 4\pi \left(R_1 + R_2\right)^2 \left(\dot{R}_1 + \dot{R}_2\right) \tag{4.51}$$

Due to the diluteness of the bubbles, I assume that the bubbles grow isolatedly without influence by near bubbles and the concentration of gas componets in the surrounding liquid is not so modified by the bubble growth.

For step decompression, meaning that the pressure is reduced by ΔP at $t = 0$ and kept to the reduced value, the bubbles grow in the following two ways. Viscosity-limited growth: the bubbles expand under the viscous resistance by the surrounding liquids to resolve the overpressure inside the bubbles ΔP with the chemical equilibrium. Diffusion-limited growth: the bubbles grow by the gas diffusion from the surrounding liquid to resolve the oversaturation ΔC due the decompression with the mechanical equilibrium. The bubble growth laws are provided below (see Appendix. A.1 for further details).

$$\Gamma(v,t) = \begin{cases} \left(4\sqrt{3}\pi\right)^{2/3} v_G D \Delta C v^{1/3} & \text{diffusion-limited growth} \\ \dfrac{3\Delta P}{4\eta} v & \text{viscousity-limited growth} \end{cases} \tag{4.52}$$

I choose the timescale for the non-dimensionalization as follows:

$$\tau_{growth} = \begin{cases} (4\sqrt{3}\pi)^{-2/3} \dfrac{v_0^{2/3}}{v_G D \Delta C} & \text{diffusion-limited growth} \\ \dfrac{4\eta}{3\Delta P} & \text{viscousity-limited growth} \end{cases} \tag{4.53}$$

Using these timescales, I obtain the non-dimensionalized equation for the evolution of BSD.

$$\begin{aligned} &\frac{\partial n^*}{\partial t^*} + \frac{\partial}{\partial v^*}\left(v^{*\omega} n^*\right) \\ &= \phi_0 \left\{ \frac{1}{2} \int_0^{v^*} K^*_{\text{growth}}(v^* - v'^*, v'*) n^*(v^* - v'^*, t^*) n^*(v'^*, t^*) dv'^* \right. \\ &\left. -n^*(v^*, t^*) \int_0^{\infty} K^*_{\text{growth}}(v^*, v'^*) n^*(v'^*, t^*) dv'^* \right\} \end{aligned} \tag{4.54}$$

where ω is the exponent characterizing the growth behaviour as follows:

$$\omega = \begin{cases} 1/3 & \text{diffusion-limited growth} \\ 1 & \text{viscosity-limited growth} \end{cases} \tag{4.55}$$

The non-dimensionalized form of the coalescence frequency function is

$$K^*_{\mathrm{growth}}(v_1^*, v_2^*) = 4\pi(v_1^{*1/3} + v_2^{*1/3})(v_1^{*-2/3+\omega} + v_2^{*-2/3+\omega}) \tag{4.56}$$

The non-dimensionalized equation of the BSD evolution has only one parameter, the initial volume fraction of the bubbles ϕ_0.

4.3.4 Numerical results for diffusion-limited growth

Fig. 4.7 shows the evolution of the distribution. Fig. 4.8 shows the evolution of the right edge and left edge of the distribution.

For $\phi_0 = 10^{-7}$, the distribution shifts to the right keeping its initial shape (Fig. 4.7a). Both edges of the distributions evolve as $t^{3/2}$ (Fig. 4.8), indicating isoalted growth without coalescence $\frac{dv}{dt} \propto v^{1/3}$ (Equation. 4.52). These results show that, for quite low volume fraction, the bubbles isolatedly grow without coalescence.

For $\phi_0 = 10^{-4}$, the distribution begins to widen at $t^* \sim 20$ (Fig. 4.7b), The left edge evolves as $t^{3/2}$, whereas the right edge evolves more rapidly than $t^{2/3}$ (Fig. 4.8). This indicates that the smaller bubbles grow isolatedly, whereas the larger bubbles grow and coalesce.

For $\phi_0 = 10^{-1}$, the distribution begins to widen at $t^* \sim 0.01$. and continues to widen over $t \sim 900$ (Fig. 4.7c). The left edge evolves as $t^{3/2}$, whereas the right edge seems to evolve as $t^{2/3} \ln t$ (Fig. 4.8).

The figure 4.9 shows the scaling of the moments of the distribution of bubbles. The bubble number density (BND) collapses into a single curve with the scaled time $t^* \phi_0^{2/3}$ (Fig. 4.9a). The BND decays as $t^{-3/2}\phi_0^*$ after some time has passed. The volume fraction of thhe bubbles increases as $t^{3/2}$ for low volume fraction, whereas it increases $\ln t$ for large volume fraction. I make the following empirical foramuls for the moments:

$$\phi(t)/\phi_0 = 1 + \frac{2}{3}\frac{1}{a\phi_0} \ln\left(1 + a\phi_0 t^{*3/2}\right) \tag{4.57}$$

$$\approx \begin{cases} 1 + t^{*3/2} & t^* \ll (a\phi_0)^{-2/3} \\ 1 + \frac{1}{a\phi_0} \ln t^* & t^* \gg (a\phi_0)^{-2/3} \end{cases} \tag{4.58}$$

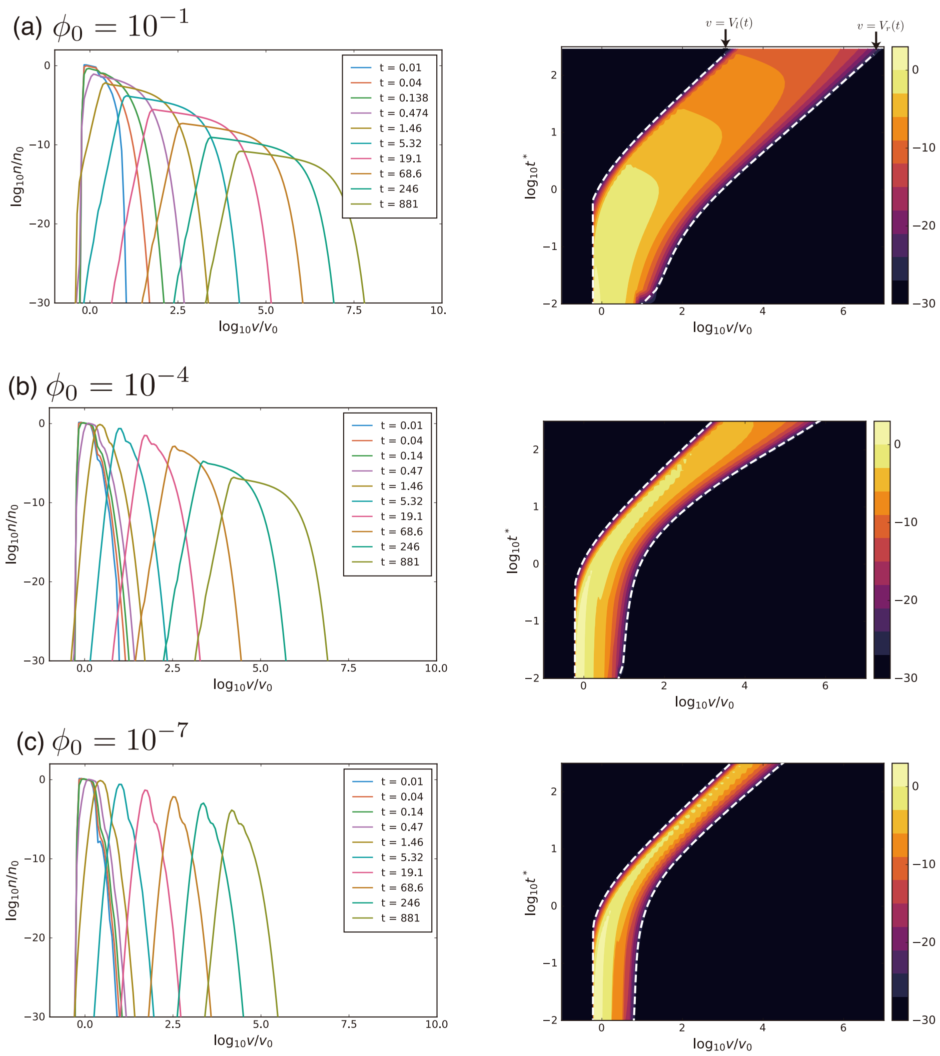

Fig. 4.7: Evolution of the bubble size distribution in a system experiencing growth and coalescence driven by diffusion-limited growth, for three initial volume fractions: (a) $\phi_0 = 10^{-1}$, (b) $\phi_0 = 10^{-4}$, and (c) $\phi_0 = 10^{-7}$. The left panels display the size distribution as a function of volume and number. The curves represent the distribution profiles at different times, as indicated in the legend. The right panels display the size distribution as a function of volume and time. The white dashed lines indicate the minimum volume, V_l, and the maximum volume, V_r. The numbers are normalized by the initial number, n_0, and the volumes are normalized by the initial volume, v_0. Both horizontal and vertical axes are displayed on a logarithmic scale.

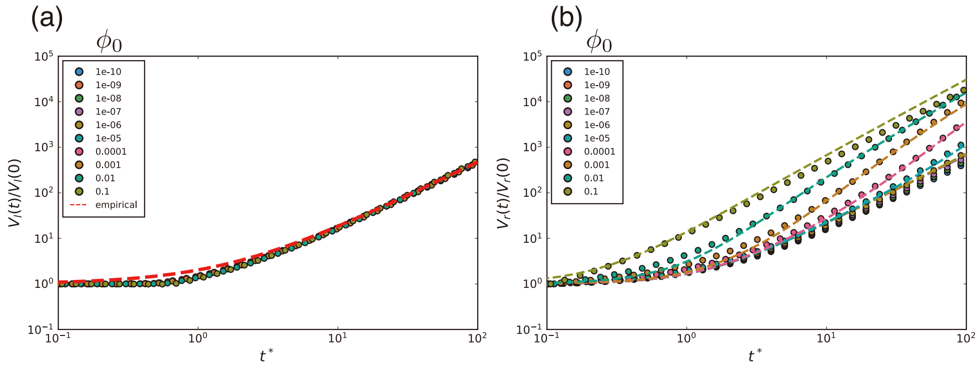

Fig. 4.8: Evolution of the maximum and minimum volumes of the bubble size distribution in growth and coalescence driven by diffusion-limited growth, (a) $V_l(t)$, (b) $V_r(t)$. The numerical results are represented by the markers, both normal- ized by their respective initial values $V_l(0)$ and $V_r(0)$. The marker color represents the initial volume fractions as indicated in the legend box. The dashed lines showsthe empirical curves given by Equations (4.61) and (4.62). Both the horizontal and vertical axes use logarithmic scales.

$$N(t)/N(0) = \left\{1 + b\phi_0 t^{*3/2}\right\}^{-1} \tag{4.59}$$

$$\approx \begin{cases} 1 & t^* \ll (b\phi_0)^{-2/3} \\ b^{-1}\phi_0^{-1}t^{*-3/2} & t^* \gg (b\phi_0)^{-2/3} \end{cases} \tag{4.60}$$

$$V_l(t)/V_l(0) = (1 + 0.6t^*)^{3/2} \tag{4.61}$$

$$V_r(t)/V_r(0) = \left[1 + \frac{1}{33.5\phi_0} \ln\left(1 + 22.3\phi_0 t^{*3/2}\right)\right]\left(1 + 92.8\phi_0 t^{*3/2}\right) \tag{4.62}$$

where the constants a and b are determined from fitting and are $a = 40$ and $b = 10^2$.

4.3.5 Numerical results for viscous-limited growth

Fig. 4.10 shows the evolution of the distribution. Fig. 4.12 shows the evolution of the moments of the distribution.

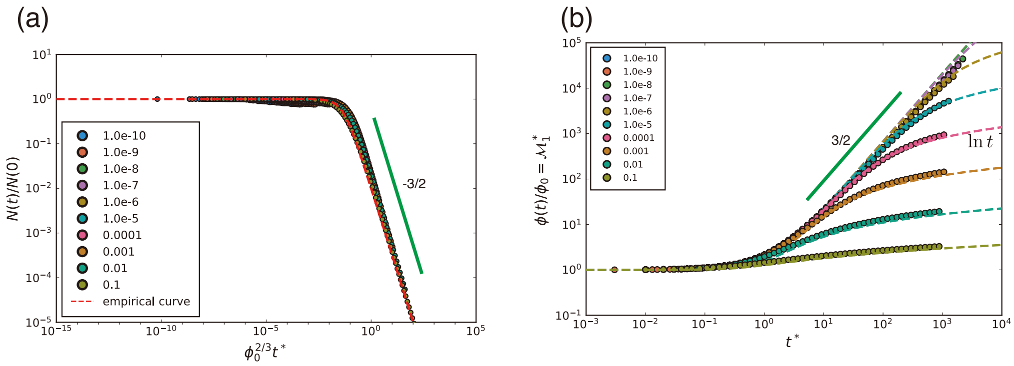

Fig. 4.9: Evolution of the moments of the bubble size distribution in growth and coalescence driven by diffusion-limited growth. (a) Evolution of bubble number density, represented by the markers. The dashed line shows the empirical curve given by Equation (4.59). The green bold line represents the power-law $N \propto t^{-3/2}$. The time axis is scaled by the initial volume fraction $\phi_0^{2/3}$. (b) Evolution of bubble volume fraction, represented by the blue line. The dashed line shows the empirical curve given by Equation (4.57). The green bold line represents the power-law $\phi \propto t^{3/2}$. The marker color represents the initial volume fractions as indicated in the legend box. Both the horizontal and vertical axes use logarithmic scales.

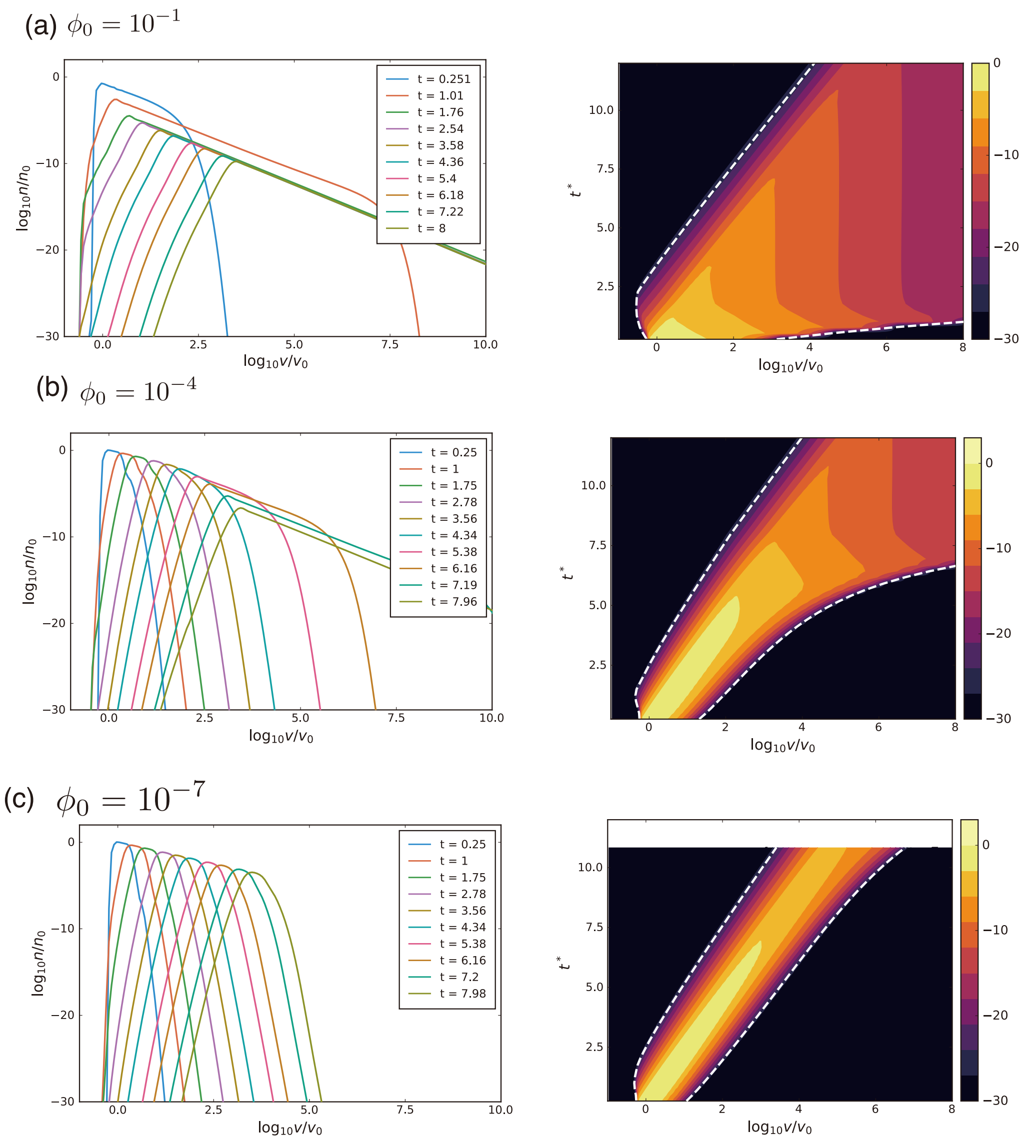

Fig. 4.10: Evolution of the bubble size distribution in a system experiencing growth and coalescence driven by viscosity-limited growth, for three initial volume fractions: (a) $\phi_0 = 10^{-1}$, (b) $\phi_0 = 10^{-4}$, and (c) $\phi_0 = 10^{-7}$. The left panels display the size distribution as a function of volume and number. The curves represent the distribution profiles at different times, as indicated in the legend. The right panels display the size distribution as a function of volume and time. The white dashed lines indicate the minimum volume, V_l, and the maximum volume, V_r. The numbers are normalized by the initial number, n_0, and the volumes are normalized by the initial volume, v_0. Both horizontal and vertical axes are displayed on a logarithmic scale.

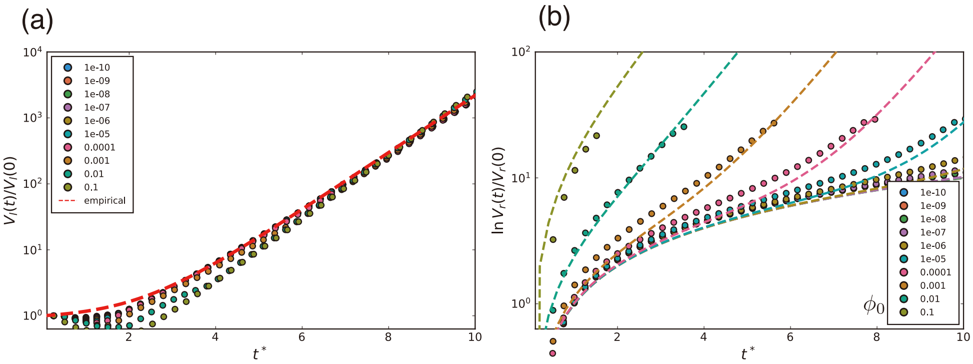

Fig. 4.11: Evolution of the maximum and minimum volumes of the bubble size distribution in growth and coalescence driven by viscosity-limited growth, (a) $V_l(t)$, (b) $V_r(t)$. The numerical results are represented by the markers, both normalized by their respective initial values $V_l(0)$ and $V_r(0)$. The marker color represents the initial volume fractions as indicated in the legend box. The dashed lines showsthe empirical curves given by Equations (4.65) and (4.66). The only vertical axes use logarithmic scale and the logartihmic values are plotted in (b).

For $\phi_0 = 10^{-7}$, the distribution shifts to the right while keeping its initial shape. Both edges of the distributions evolve as e^t (Fig. 4.8a), This indicates that the bubbles isolatedly grow as $\frac{dv}{dt} \propto v$ (Equation 4.52). For $\phi_0 = 10^{-4}$, the distribution begins to widen at $t^* \sim 1$ and shows the power-law with a slope of -2. The left edge evolve as e^t, whereas the right edge evolves rapidly than e^t (Fig. 4.8b). This indicates that the bubbles grow and coalesce. For $\phi_0 = 10^{-1}$, the distribution begins to widen at $t^* \sim 0.2$ and shows the power-law.

The volume fraction of the bubbles exponentially increase independent of ϕ_0. The BND decreases more rapidly than e^{-t}. Fig. 4.12 shows the scaling of the distribution's moments. The BND decreases faster than exponentially, in a form of e^{-ae^t}, and decreases more rapidly in a shorter time for larger initial volume fraction (Fig. 4.12a,b). The bubble number density increases exponentially regardless of the initial value (Fig. 4.12c). Based on these scaling results, the following empirical formula was created, with constants determined through fitting.

$$\phi(t)/\phi_0 = M_1^* = e^{t*} \tag{4.63}$$

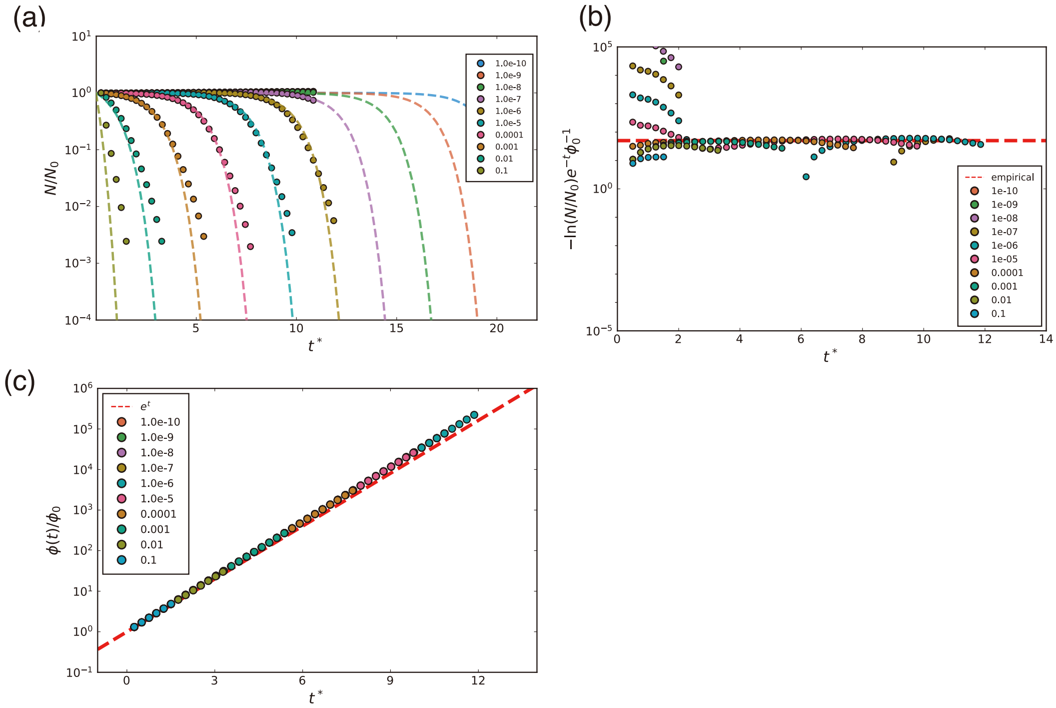

Fig. 4.12: Evolution of the moments of the bubble size distribution in growth and coalescence driven by viscosity-limited growth. (a) Evolution of bubble number density, represented by the markers. The dashed line shows the empirical curve given by Equation (4.64). (b) The scaled value of the bubble number density to confirm the emprical formula. (c) Evolution of bubble volume fraction, represented by the blue line. The dashed line shows the empirical curve given by Equation (4.63). The marker color represents the initial volume fractions as indicated in the legend box. The only vertical axes use logarithmic scale.

$$N(t)/N(0) = \exp\left(50\phi_0(1 - e^{t*})\right) \tag{4.64}$$

$$V_l(t)/V_l(0) = e^t \tag{4.65}$$

$$V_r(t)/V_r(0) = \exp\left(t^* + 80\phi_0(e^{t*} - 1)\right) \tag{4.66}$$

4.3.6 Bubble growth under continuous decompression

We assume that gas bubbles with volume v and internal gas pressure P_g are placed in a liquid with pressure P.

The pressure of the liquid is gradually reduced at a constant decompression rate $\dot{P}$ as:

$$P(t) = P_0 - |\dot{P}|t \tag{4.67}$$

where P_0 is the initial pressure.

The gas pressure is assumed to be balanced with the liquid pressure in chemical equilibrium

$$P_g(t) = P(t) \tag{4.68}$$

where the contribution to the pressure from the interfacial tension is neglected.

The gas is assumed to be an ideal gas and kept its temperature during the decompression:

$$\frac{dv}{dt} = -\frac{1}{P_g}\frac{dP_g}{dt}v \tag{4.69}$$

Equations (4.67), (4.68), and (4.69) yield

$$\frac{dv}{dt} = \frac{|\dot{P}|}{P_0 - |\dot{P}|t}v \tag{4.70}$$

Substituting this Equation into Equation (4.56) yields

$$K_{\text{growth}} = \frac{4\pi}{3}\frac{|\dot{P}|}{P(t)}(v_1^{1/3} + v_2^{1/3})^3 \tag{4.71}$$

Here, we choose the time-scale for nondimensionalization as:

$$\tau_{\text{growth}} = \frac{P_0}{|\dot{P}|} \tag{4.72}$$

Then, the nondimensionalized collision frequency is

$$K^*_{\text{growth}} = (1-t^*)^{-1}\left(v_1^{*1/3} + v_2^{*1/3}\right)^2\left(v_1^{*1/3} + v_2^{*1/3}\right) \tag{4.73}$$

The non-dimensionalized equation for the evolution of the BSD is given as:

$$\begin{aligned}
&\frac{\partial n^*}{\partial t^*} + \frac{\partial}{\partial v^*}(vn^*) \\
&= \phi_0\left\{\frac{1}{2}\int_0^{v^*} K^*_{\text{growth}}(v^*-v^{'*}, v'*)n^*(v^*-v^{'*}, t^*)n^*(v^{'*}, t^*)dv^{'*}\right. \\
&\left.-n^*(v^*, t^*)\int_0^{\infty} K^*_{\text{growth}}(v^*, v^{'*})n^*(v^{'*}, t^*)dv^{'*}\right\}
\end{aligned} \tag{4.74}$$

We introduce a new time variable t' for simplifying the above equation.

$$t' = \ln\left(\frac{1}{1-t^*}\right) \tag{4.75}$$

Then, we have the following transformed equation:

$$\begin{aligned}
&\frac{\partial n^*}{\partial t'} + \frac{\partial}{\partial v^*}(vn^*) \\
&= \phi_0\left\{\frac{1}{2}\int_0^{v^*} K'_{\text{growth}}(v^*-v^{'*}, v'*)n^*(v^*-v^{'*}, t')n^*(v^{'*}, t')dv^{'*}\right. \\
&\left.-n^*(v^*, t')\int_0^{\infty} K'_{\text{growth}}(v^*, v^{'*})n^*(v^{'*}, t')dv^{'*}\right\}
\end{aligned} \tag{4.76}$$

where the collision frequency is defined as

$$K'_{\text{growth}} = 4\pi\left(v_1^{*1/3} + v_2^{*1/3}\right)^2\left(v_1^{*1/3} + v_2^{*1/3}\right) \tag{4.77}$$

When t is replaced by t' (4.75) in equations (4.76) and (4.77), they take the same form as the equations for viscosity-limited growth (4.54), (4.55), and (4.56). As a result, the solutions of the transformed equations has the same form as the solutions for viscosity-limited growth. From Equations (4.63), (4.64), (4.65), and (4.66), we have the following empirical formulas:

$$\phi(t)/\phi_0 = \frac{1}{1-t^*} \tag{4.78}$$

$$N(t)/N(0) = \exp\left(\frac{50}{1-t^*}\right) \tag{4.79}$$

$$V_l(t)/V_l(0) = \frac{1}{1-t^*} \tag{4.80}$$

$$V_r(t)/V_r(0) = \frac{1}{1-t^*}\exp\left(80\phi_0\frac{t^*}{1-t^*}\right) \tag{4.81}$$

4.3.7 Self-similar scaling

As shown in the numerical results (e.g; Fig.4.4a), the well-developed size distribution shows self-similar behavior in time and volume. The size distribution would be represented by a scaling function $f(x)$ with the characteristic number density V_*^2/ϕ [27][28][29] as follows:

$$n(v,t) = \begin{cases} \dfrac{\phi(t)}{V_*(t)^2} f\left(\dfrac{v}{V_*(t)}\right) & V_l(t) < v < V_r(t) \\ 0 & \text{otherwise} \end{cases} \tag{4.82}$$

Here, the characteristic volume V_* is chosed as:

$$V_*(t) = \mathcal{M}_2/\mathcal{M}_1 \tag{4.83}$$

The self-similar representation (4.82) is useful for the analytical discussions.

To obtain the scaling function $f(x)$, I use the numerical results in Section.4.3.1, Section.4.3.2, Section.4.3.4, and Section.4.3.5. I choose the numerical data of the size distribution for the later time such that $V_*(t) > 10v_0$ indicating the bubbles have coalesced multiple times. For the coalescence of ascending bubbles, I choose the data for the time close to the critical time t_c^*.

For coalescence of ascending bubbles, Fig.4.13 (left) shows the evolution of the size distribution at the time close to $t_c^*\phi_0 \approx 4.72$. Fig.4.13 (right) shows the normalized size distribution using the moments $V_*(t), \phi(t)$. The size distributions at different times collapse into one curve, which indicates that Equation (4.82) holds and the collapsed curve is $f(x)$. $f(x)$ seems to be a curve consists of power-law and exponential curves. The following empirical formula was thus obtained through fitting:

$$f_{\mathrm{buo}}(x) = 0.0357x^{-2.01}\exp\left(-0.0441x^{0.958}\right) \tag{4.84}$$

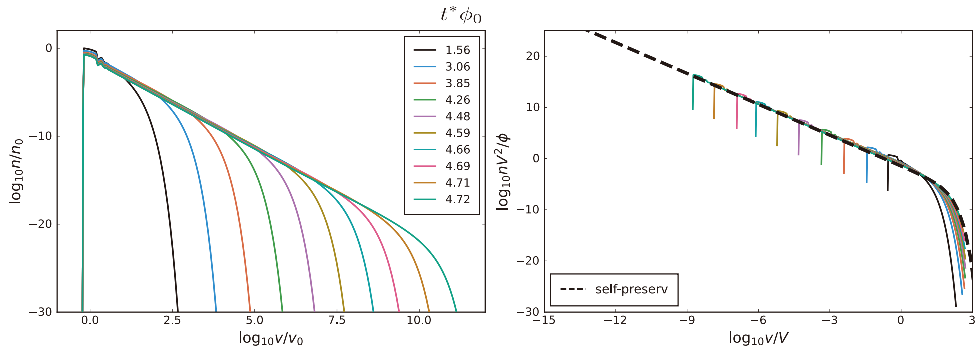

Fig. 4.13: The left panel displays the evolution of the bubble size distribution due to coalescence driven by buoyancy. The right panel shows the size distributions resacled from the left panel data, using the characteristic volume V_*, defined in Equation (4.83) and the number $\frac{\phi(t)}{V_*^2(t)}$. The dashed curves in the right panel show the empirical scaling function given by Equation (4.84). Both horizontal and vertical axes are displayed on a logarithmic scale.

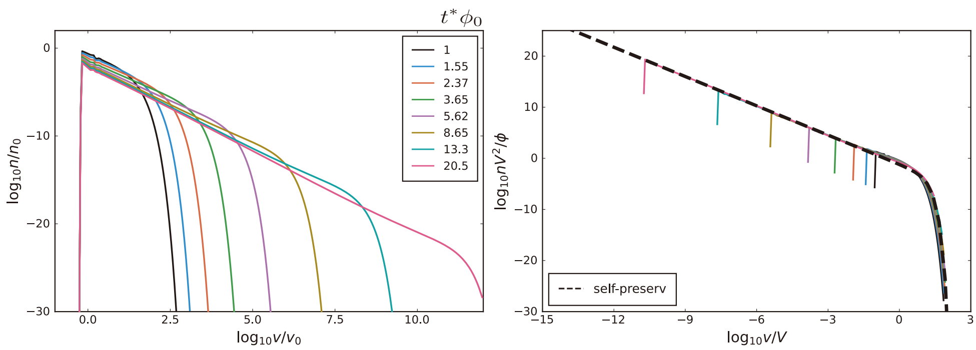

Fig. 4.14: The right panel displays the evolution of the bubble size distribution due to coalescence driven by shear. The left panel shows the size distribution resacled from the left panel data, using the characteristic volume V_*, defined in Equation (4.83) and the number $\frac{\phi(t)}{V_*^2(t)}$. The dashed curves in the right panel show the empirical scaling function given by Equation (4.85). Both horizontal and vertical axes are displayed on a logarithmic scale.

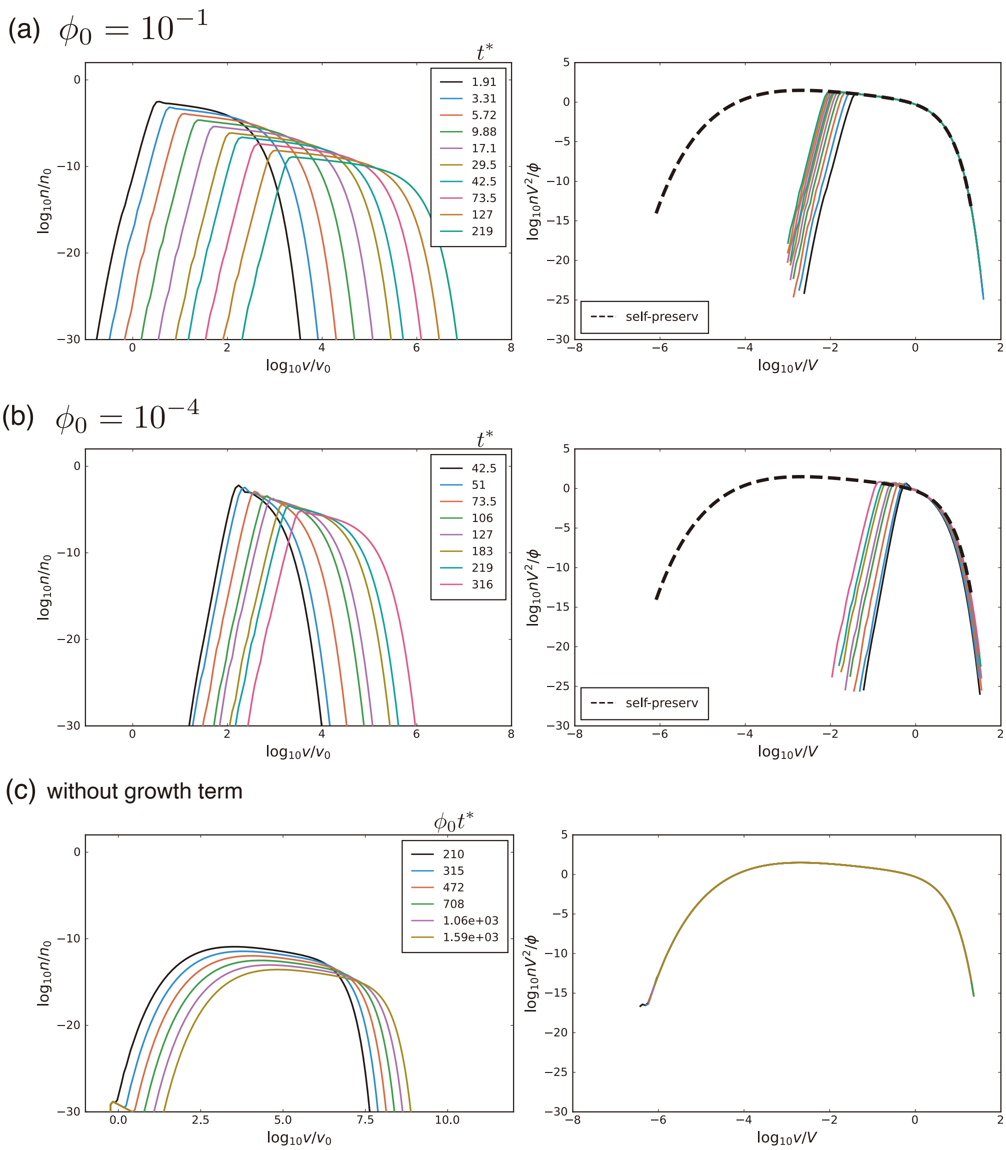

Fig. 4.15: The left panels displays the size distribution versus volume and number due to growth and coalescence driven by diffusion-limited growth, for initial volume fractions (a) $\phi_0 = 10^{-1}$, (b) $\phi_0 = 10^{-4}$, (c) the results from the calculation without the growth term in Equation (4.54). The right panels shows the size distribution resacled from the left panels data, using the characteristic volume V_*, defined in Equation (4.83) and the number $\frac{\phi(t)}{V_*^2(t)}$. The dashed curves in the right panel show the empirical scaling function given by Equation (4.86). Both horizontal and vertical axes are displayed on a logarithmic scale.

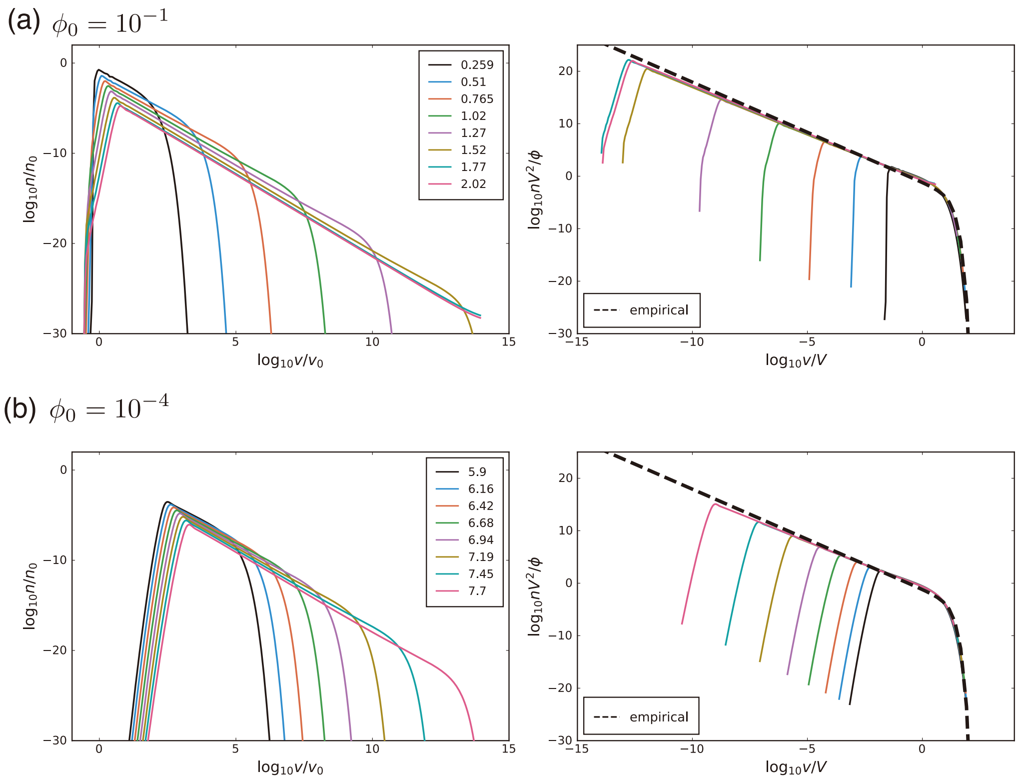

Fig. 4.16: The left panels displays the size distribution versus volume and number due to growth and coalescence driven by viscosity-limited growth, for initial volume fractions (a) $\phi_0 = 10^{-1}$, (b) $\phi_0 = 10^{-4}$. The right panels shows the size distribution resacled from the left panels data, using the characteristic volume V_*, defined in Equation (4.83) and the number $\frac{\phi(t)}{V_*^2(t)}$. The dashed curves in the right panel show the empirical scaling function given by Equation (4.87). Both horizontal and vertical axes are displayed on a logarithmic scale.

For coalescence of bubbles in shear flow, Fig.4.14 (left) shows the evolution of the size distribution and Fig.4.13 (right) shows the normalized size distribution. Similarly, the curve is fitted as a product of power-law and exponential curve:

$$f_{\text{shear}}(x) = 0.066x^{-1.9} \exp\left(-0.074x^{1.4}\right) \tag{4.85}$$

For coalescence of bubbles with diffusion-limited growth, Fig.4.15 shows the evolution of the size distribution and the normalized size distrubtions for (a) $\phi_0 = 10^{-1}$, (b) $\phi_0 = 10^{-4}$ and (c) without the growth term in Equation (4.54). I found that the normalized functions in (a) $\phi_0 = 10^{-1}$ and (b) $\phi_0 = 10^{-4}$ is collapsed on the normalized function in (c) without the growth term. (the right palnel in Fig.4.15). The curve is fitted given by the following empirical formula:

$$f_{\text{diff}}(x) = x^{-1.0} \exp\left[-1.4(x-1) - 0.49(x^{-0.3} - 1)\right] \tag{4.86}$$

For coalescence of bubbles with viscosity-limited growth, Fig.4.16 shows the evolution of the size distribution and the normalized size distributions for $\phi_0 = 10^{-1},\ 10^{-4}$. The normalized size distribution appears to collapse into a single curve, which is close to the curve for shear motion.

$$f_{\text{visc}}(x) = 0.066x^{-1.91} \exp\left(-0.074x^{1.4}\right) \tag{4.87}$$

For coalescence of expanding bubbles under continuous decompression, If the time variable t is replaced with $t' = \ln\left(\frac{1}{1-t}\right)$, the size evolution follows the same dynamics as viscosity-limited growth shown as Equation (4.76). The scaling function is thus identical to Equation (4.87):

$$f_{\text{expand}}(x) = f_{\text{visc}}(x) \tag{4.88}$$

4.4 Discussions

4.4.1 Coalescence Behaviour

Table. 4.1 summarize the numerical results for Section. 4.2. τ is the time unit for the non-dimensionlization depending on the driving force of the coalescence. The minimum volume of the distribution V_l evolves as the growth law for isolated growing bubbles $\frac{dV_l}{dt} \sim V_l^{\omega}$. V_l is constant for ascending and shear motion because

Table 4.1: Summary of the numerical results and empirical formulas

	τ	power	N	ϕ	V_l	V_r
Buoyancy	$\frac{\mu}{\rho g R_0}$	-2	$e^{-a(t^*\phi_0)^{1.85}}$	1	1	$\phi_0^{-3.4}(t_c^* - t^*)^{-3.4}$
Shear	$\dot{\gamma}^{-1}$	-2	$(t^*\phi_0)^{-1}$	1	1	$e^{2(t^*\phi_0)^{0.82}}$
Diffusion-limited	$\frac{R_0^2}{D}$	-0.5	$(t^*\phi_0^{2/3})^{-3/2}$	$\phi_0 \ln t^*$	$t^{*3/2}$	$t^{*3/2}\ln(t^*\phi_0^{2/3})$
Viscosity-limited	$\frac{\mu}{P_0}$	-2	$\exp(-b\phi_0 e^{t^*})$	e^{t^*}	e^{t^*}	$\exp(c\phi_0 e^{t^*})$
Isothermal-expansion	$\frac{P_0}{\lvert\dot{P}\rvert}$	-2	$\exp(-\frac{b\phi_0}{1-t^*})$	$(1-t^*)^{-1}$	$(1-t^*)^{-1}$	$\frac{1}{1-t^*}\exp(\frac{c\phi_0}{1-t^*})$

the growth term is neglected. The maximum volume V_r evolves orderly as $t^{3/2}\ln t$ for the diffusion-limited growth, whereas it evolves exponetially for the other three cases. The well developed distriution is powerlaw with a slope of -0.5 for the diffusion-limited growth and power-law with a slope of -2 otherwise.

Table 4.2: List of the exponents of the collision kernels

	kernel	μ	ν	ω
Buoyancy	$(v_1v_2)^{1/3}\lvert v_1^{2/3} - v_2^{2/3}\rvert$	$1/3$	1	1
Shear	$(v_1v_2)^{1/3}(v_1^{1/3} + v_2^{1/3})$	$1/3$	$2/3$	1
Diffusion-limited	$(v_1^{1/3} + v_2^{1/3})^2(v_1^{-1/3} + v_2^{-1/3})$	$-1/3$	$2/3$	$1/3$
Viscosity-limited	$(v_1^{1/3} + v_2^{1/3})^2(v_1^{1/3} + v_2^{1/3})$	0	1	1

The essential factors for coalescnece and growth are the collision-frequency K and the growth rate Γ. These functions can be simplified as:

$$K(v_1, v_2) \sim v_1^{\mu} v_2^{\nu} \quad \text{for } v_1 \ll v_2 \tag{4.89}$$

$$\Gamma(v) \sim v^{\omega} \tag{4.90}$$

These exponents μ, ν, ω characterize the long-time evolution of the size distribution[30]. Table. 4.2 summarize the exponents of the four coalesncece cases.

The evolution style of the size distribution is classified by the exponents sum $\gamma = \mu + \nu$ [24]. The characteristic volume V_* qualitatively evolves as $\frac{dV_*}{dt} \propto V_*^{\gamma}$. For ascending bubbles $\gamma = 4/3 > 1$, V_* diverges logrithmically with in a finite time. For shear and viscosity-limited growth $\gamma = 1$, V_* diverges exponentially with time. For diffusion-limited growth $\gamma = 1/3 < 1$, V_* increases orderly. These behaviors are consistent with the qualitative behavior of V_r (Table. 4.1).

4.4.2 Distribution Width

I introduce the width of the size distribution as the ratio of the maximum and minimum volumes:

$$\delta(t) = \frac{V_r(t)}{V_l(t)} \tag{4.91}$$

The width δ is a quantity representing the degree of coalescence because δ does not change when bubbles grow independently. The size width is represented for each case of coalescence as follows from Table. 4.1.

$$\delta_{\text{buo}}(t)/\delta_0 \approx 10^{3.7}(4.73 - t^*\phi_0)^{-3.4} \tag{4.92}$$

$$\delta_{\text{shear}}(t)/\delta_0 \approx e^{2.0(\phi_0 t)^{*0.82}} \tag{4.93}$$

$$\delta_{\text{diff}}(t)/\delta_0 \approx \ln\left(\phi_0 2/3t^*\right) \tag{4.94}$$

$$\delta_{\text{visc}}(t)/\delta_0 \approx \exp\left(80\phi_0 e^{t*}\right) \tag{4.95}$$

$$\delta_{\text{expand}}(t)/\delta_0 \approx \exp\left(\frac{80\phi_0}{1 - t^*}\right) \tag{4.96}$$

where the initial width is defined as $\delta_0 = V_r(0)/V_l(0)$, and $t^* \gg 1$ is assumed. Using the empirical formulas, I could estimate the non-dimensional time t^* from the distribution width δ. This is useful for understanding the vesicle texture of the pyroclasts.

Chapter 5

Implication

In this chapter, I discuss bubble coalescence during volcanic eruption from the results in Chapter. 4.

5.1 Bubble coalescence just after nucleation

I examine the coalescence of bubbles in magma during volcanic eruptions. I focus on the growing process just after the nucleation of the bubbles in the deep region. Toramaru (1995)[1] numerically predicted the ascenidng magma nucleates at once in the deep part of the conduit, and the nucleated bubbles grow due to their overpressure and oversaturation.

First, I describe the equilibrium profiles before discussing the non-equilibrium growing process. The pressure of the magma is assumed to be the static pressure as:

$$p(z) = \rho g z \tag{5.1}$$

where $\rho = 2.5 \times 10^3\ \mathrm{kgm^{-3}}$ is the melt density, and z is the depth from the surface of the volcano. I assume that gas in bubbles follows the equation of state of the ideal gas. At $z < -2\mathrm{km}$, the magma would be dilute suspension of bubbles with small volume fraction. The solubility law of the water contents in the magma is as follows:

$$n_g = \frac{n_0 - sp^m}{1 - p^m} \tag{5.2}$$

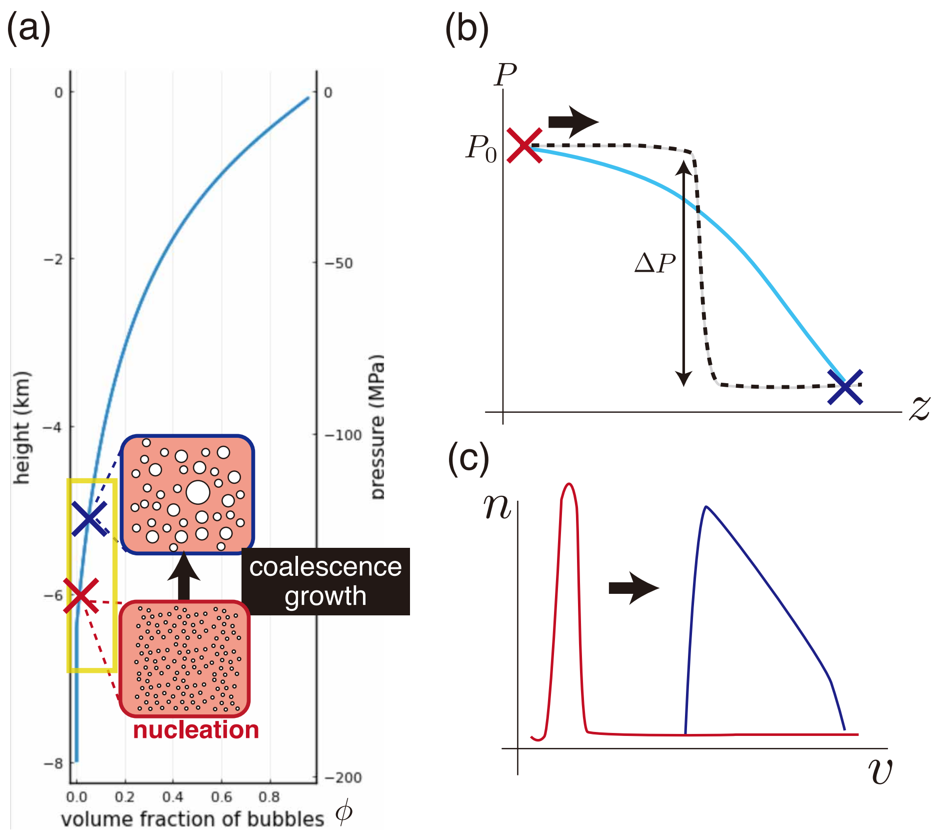

Fig. 5.1: (a) The volume fraction of bubbles plotted against depth and static pressure. The water content in the magma is 5% by mass, and the magma temperature is $1,000$ K. The red cross represents the initial state just after nucleation, and the blue cross represents the final state after growth and coalescence. (b) Schematic diagram of pressure change focusing on the yellow region in (a). The red and blue crosses correspond to the initial and final states in (a), respectively. The solid line represents the curve of the change in equilibrium pressure with height. The dashed line represents an approximation of the pressure change with step decompression of ΔP. (c) Schematic representation of the size distribution in the initial and final states.

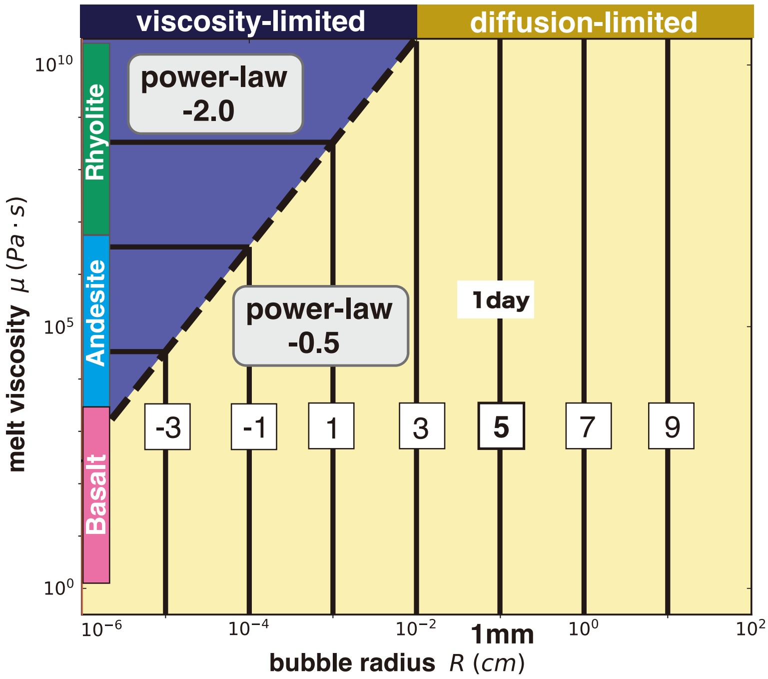

Fig. 5.2: The coalescence time-scale of growing bubbles as a function of bubble radius and melt viscosity. The solid lines indicate contours of the coalescence time. The labels on the viscosity axis represent the typical viscosity range for basalt, andesite, and rhyolite. The purple region represents the region where coalescence is limited by viscosity, while the yellow region represents the region where coalescence is limited by diffusion. The gray region represents the region where no coalescence occurs, with a timescale larger than the eruption time-scale of 10^5 seconds. The parameters used in the calculation are an initial volume fraction of $\phi_0 = 10^{-3}$, a surrounding pressure of $p = 100$ MPa, and a diffusivity of $D = 10^{-9}$ $\mathrm{m^2/s}$.

where $s = 4 \times 10^{-6}$, $m = 0.5$. The volume fraction of the gas in the magma is given as:

$$\phi = \frac{n_g RT}{p} \left(\frac{n_g RT}{p} + \frac{1 - n_g}{\rho} \right)^{-1} \tag{5.3}$$

Using Equations (5.1), (5.2), and (5.3), we plot the height profile of the bubble volume fraction in the magma at the static pressure (Fig. 5.1a).

Next, I estimate the time-scale of the coalescence of the growing bubles just after their nucleation. The pressure of the ascending magma is continuously reduced. We approximate the pressure evolution as the step decompression (the dashed curve in Fig. 5.1b)[31]. Under the step decompression, the bubbles grow either due to viscosity-limited growth or diffusion-limited growth to release the overpressure and oversaturation. The growth and coalesce of bubbles stop when the overpressure inside the bubble is released. I obtain the coalescence time-scales for viscosity-limited growth and diffusion-limtied growth using the empirical formulas in Chapter. 4.

$$\tau_{\text{visc}} = \ln\left(0.02\phi_0^{-1}\right) \mu / p_0 \tag{5.4}$$

$$\tau_{\text{dif}} = \phi_0^{-2/3} R_0^2 / D \tag{5.5}$$

where p_0 is the initial pressure, R_0 is the initial radius, and ϕ_0 is the initial volume fraction. The coalescence time-scale would be the maximum of the two time-scales due to the competition between the two growth styles:

$$\tau_{\text{coale}} = \max\left(\tau_{\text{visc}}, \tau_{\text{dif}}\right) \tag{5.6}$$

Fig.5.2 plots the coalescence time-scale as a function of bubble radius and melt viscosity. The plotting parameters are summerized in the figure caption. For high viscosity magma, such as andesite and rhyolite, viscosity-limited growth dominates and drives rapid coalescence, forming a power-law size distribution with a slope of -2. For low viscosity magma, such as basalt, diffusion-limited growth dominates and drives orderly coalescence, forming a power-law size distribution with a slope of -0.5.

Applying these estimations directly to the vesicle texture of pyroclasts is still difficult. This is because the assumption is made for a step decompression, but in reality, the pressure decreases continuously, leading to more complicated growth of the bubbles. Additionaly, these discussions only focus on the shallow part of the magma conduit, but as the magma approaches the shallower part, the bubbles start to expand isothermally due to the rapid reduction in pressure, causing the magma to fracture. Therefore, we need to consider more complex factors when interpreting the vesicle texture in pyroclasts.

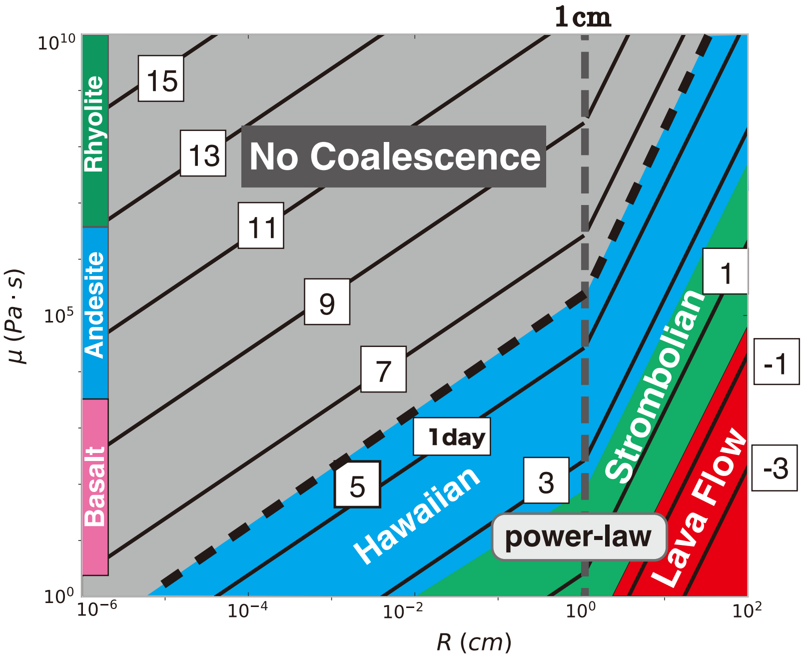

Fig. 5.3: The coalescence time-scale of ascending bubbles as a function of their radius and the viscosity of the melt. The solid lines indicate contours of the coalescence time with the blue region typical for lava flows, the green region for Strombolian eruptions, and the yellow region for Hawaiian eruptions. The viscosity axis is labeled with the typical viscosity range for basalt, andesite, and rhyolite. The gray region indicates a region of no coalescence, where the timescale is greater than the eruption time-scale of 10^6 sec. The calculations were performed with an initial volume fraction of $\phi_0 = 10^{-1}$ and an interfacial tension of $\sigma = 0.1$ N/m.

The coalescence of bubbles driven by buoyancy is significant in basaltic eruptions due to their low viscosity. As discussed in Chapter. 4, ascending bubbles coalesce violently and the maximum bubble volume $V_r(t)$ diverges in a finite time, indicating the formation of a giant bubble comparable to the system size such as the conduit radius. The critical time of the coalescence t_c is given as (Equation. 4.34):

$$t_c \sim 4.7\phi_0^{-1}\frac{\mu}{\rho g R} \tag{5.7}$$

In Chapter. 2, I have showed that the large bubbles deform and attract each other, leading to effective coalescence. The deformation of the bubbles is controlled by the Bond number:

$$\mathrm{Bo} = \frac{\rho g R^2}{\sigma} \tag{5.8}$$

I have found that the deformation increases the collision-frequency by a factor of Bo if $\mathrm{Bo} > 1$ Equation. (2.58). The coalescence time-scale is thus given by:

$$\tau_{\mathrm{coale}} \approx \begin{cases} \phi_0^{-1}\dfrac{\mu}{\rho g R} & \mathrm{Bo} < 1 \\ \phi_0^{-1}\dfrac{\mu}{\rho g R}\mathrm{Bo}^{-1} & \mathrm{Bo} > 1 \end{cases} \tag{5.9}$$

The initial volume fraction is assumed to be $\phi_0 = 0.1$. We assume that the ascending magma reaches the vent within 10^6 sec. Fig.5.3 plots the time-scale for buoyancy-driven coalescene of the bubbles as a function of bubble radius and melt viscosity. For basalt and larger bubbles than $0.1\mathrm{mm}$, the bubbles coalesce before erupts from the vent. At $R \approx 1\mathrm{cm}$, the behavior of the time-scale changes at from R^{-1} to R^{-3} due to deformation (Equation 5.9). The parameter region where coalescence occurs rapidly within 10 sec appears in regions where the radius exceeds 1 cm is found.

It is known that the duration of basaltic eruptions ranges from $10 - 10^2$ sec in Strombolian eruptions to $10^2 - 10^6$ sec in Hawaiian eruptions[32]. Parfitt and Wilson (1995)[33][34] discuss that the coalescence of bubbles during eruption would contribute to the difference of the eruption styles. The coalesced bubbles would escape from the surrounding magma due to their large ascending velocities, generating the heterogeneosu gas profile in conduit. Our studies can give the reasonable estimation of the gas migration from the coalescence time-scale (Equation. 5.9). Note that the intermittent formation and rise of bubbles with a diameter of 5 m at a lava lake was observed over a period of 150 sec[35].

Chapter 6

Conclusion

Understanding the dynamics of the eruption is also important by changing the rheology of the magma or the critical value of fragmentation. Our findings contribute to the understanding of bubble texture in pyroclasts and gas dynamics in conduit from the perspective of bubble size distribution.

First, the interaction of two ascending bubbles with deformation was studied (Chapter. 2). The calculation of the trajectory and shape revealed that the mechanism of attraction of two deformed bubbles under buoyancy. One bubble deforms due to the shear stress of the flow created by the ascending motion of the other bubble. This shape anisotropy leads the incline of the ascending direction to the other bubble, resulting in the attraction. The coalescence frequency function, taking into account the effect of deformation, was analytically determined.

Next, I study the coalescence of bubbles driven by the various driving forces, such as buoyancy, shear, and growth. Using the equation of motion, I derived the collision frequency function for the several conditions (Chapter. 3). I investigated the time evolution of bubble size distribution using the obtained coalescence frequency function, numerically (Chapter. 4). I studied the time scale and shape of the distribution and the development of moments in detail. As a result, I found that, for buoyancy, shear, viscosity-limited growth, and isothermal expansion, bubbles rapidly coalesce and form a power-law with a slope of -2. I also found that, for diffusion-limited growth, bubbles orderly coalesce and form a power-law distribution with a slope of -0.5. From the numerical calculations, I provided empirical formulas for the size distribution and moments.

Finally, the comparison of eruption time scale and coalescence time scale was discussed in regards to volcanic eruption bubble coalescence (Chapter. 5). For coalescence driven by bubble growth, at $2-6$ km depth from the surface, the bubbles may grow and coalesce due to their over-saturation and overpressure, leading to viscosity-limited, diffusion-limited coalescence investigated in Chapter. 4. This may impose constraints on the power-law often observed in the bubble textures of scoria and pumice. For coalescence driven by buoyancy, bubbles over $0.1\ \mathrm{mm}$ may rapidly coalesce to form large bubbles. Larger bubbles over $1\ \mathrm{cm}$ may coalesce faster due to the effect of deformation and may coalesce within $10\ \mathrm{sec}$. These coalescences may cause migration of bubbles and result in inhomogeneity of gas profile in conudit. Thus, these time scales may be related to the transition of eruption patterns such as Hawaiian and Strombolian.

Acknowledgement

I would like to express my gratitude to my supervisor, Atsushi Toramaru, for his invaluable support and daily discussion throughout my research. His lecture has made me start a career as a volcanologist. I learned from him how we observe and study the nature as a scientist. I am also grateful to Masatoshi Ohashi for his critical comments to my research, as well as his encouragement to my daily life. I would like to thank Atsuko Namiki and Mie Ichihara for their insightful discussions to my work. I would also like to acknowledge all the students in the Laboratory for Group of Petrology and Volcanology. Finally, I deeply appreciate to my parents, Yuichi Maruishi and Hiroko Maruishi. This study was supported by JSPS KAKENHI Grant No. 21J11749, Grant-in-Aid for JSPS Research Fellow.

Appendix A

Appendix

A.1 Bubble Growth

A.1.1 diffusion-limited growth

I briefly explain the diffusion-limited growth of bubbles. Assuming that mechanical equilibrium is maintained, I consider the case where the concentration difference $\Delta C = C_\infty - C_R$ is constant. I examine a steady and spherical symmetric concentration field $C(r)$. The diffusion equation is then reduced to the following form:

$$\nabla^2 C = 0 \tag{A.1.1}$$

Given that the concentration field at the particle surface C_R and at infinity C_∞ at infinity, I can express the concentration field as:

$$C(r) = C_\infty - \Delta C \frac{R}{r} \tag{A.1.2}$$

where v_G is the volume of a single gas component molecule, and D is the diffusivity.

In this case, considering the influx of molecules from the bubble surface, I have:

$$\frac{d}{dt}\left(\frac{4\pi}{3}R^3\right) = -4\pi R^2 I \tag{A.1.3}$$

Here, I is the diffusion flux, which can be evaluated from the concentration field as:

$$I = -v_G D \left.\frac{\partial C}{\partial r}\right|_{r=R} \tag{A.1.4}$$

This results in a growth rate that is proportional to R^{-1}, or:

$$\frac{dR}{dt} = v_G D \frac{\Delta C}{R} \tag{A.1.5}$$

This is written in terms of volume V as follows:

$$\frac{dV}{dt} = aV^{1/3} \tag{A.1.6}$$

$$a = \left(4\sqrt{3}\pi\right)^{2/3} v_G D \Delta C \tag{A.1.7}$$

A.1.2 viscosty-limited growth

In this model, it is assumed that there is a constant excess pressure $\Delta P_G = P_G - P$ within the bubble. When the mechanical equilibrium is disturbed, the bubble will grow while driven by a flow field that is in balance with the viscous resistance.

Assuming an incompressible viscous fluid, the flow field is assumed to be spherically symmetric, with velocity field $u(r)$. The continuity equation is

$$\boldsymbol{\nabla} \cdot \boldsymbol{u} = 0 \tag{A.1.8}$$

and assuming that the radial velocity at the bubble's surface is $u_r = \dot{R}$, the velocity field can be described as

$$u_r = \frac{R^2}{r^2} \dot{R} \tag{A.1.9}$$

The stress tensor in the radial direction at the bubble surface is given by

$$\sigma_{rr} = 2\eta \left.\frac{du}{dr}\right|_{r=R} \tag{A.1.10}$$

$$= -4\eta \frac{\dot{R}}{R} \tag{A.1.11}$$

Balancing this stress with the excess pressure ΔP_G yields

$$4\eta \frac{\dot{R}}{R} = \Delta P_G \tag{A.1.12}$$

which gives the solution

$$\frac{dR}{dt} = \frac{\Delta P}{4\eta} R \tag{A.1.13}$$

This is written in terms of volume V as follows:

$$\frac{dV}{dt} = aV \tag{A.1.14}$$

$$a = \frac{3\Delta P}{4\eta} \tag{A.1.15}$$

A.2 Collision rate of bubble growth with hydrodynamic interaction

With hydrodynamic interaction, $p_{12}(r,t)$ is non-steady and non-uniform. Substituting Equation (3.60) into Equation (3.64) yields

$$\frac{\partial p_{12}(r,t)}{\partial t} + G(t)\frac{\partial}{\partial r}\left(\frac{p_{12}(r,t)}{r^2}\right) = 0 \tag{A.2.16}$$

where $G(t)$ is the following funcion:

$$G(t) = R_1^2(t)\dot{R}_1(t) + R_2^2(t)\dot{R}_2(t) \tag{A.2.17}$$

Solving Equation (A.2.16) and (A.2.17) yields an analytical solution of the pair-distribution function:

$$p_{12}(r,t) = \left(1 - \frac{3}{r^3}\int_0^t G(t)dt\right)^{-2/3} \tag{A.2.18}$$

Substituting Equation (A.2.18) into Equation (3.63) yields the collision rate for growing bubbles with hydrodynamic interaction:

$$J_{12}(t) = 4\pi n_1 n_2 E(t)(R_1 + R_2)^2(\dot{R}_1 + \dot{R}_2) \tag{A.2.19}$$

where E is the collision efficiency defined as follows:

$$E(t) = \left(1 - \frac{3}{(R_1 + R_2)^3} \int_0^t G(t)dt\right)^{-2/3} \left[1 - \frac{G(t)}{(R_1 + R_2)^2 \left(\dot{R}_1 + \dot{R}_2\right)}\right] \tag{A.2.20}$$

The collision efficiency is initially

$$E(0) = 1 - \left.\frac{R_1^2 \dot{R}_1 + R_2^2 \dot{R}_2}{(R_1 + R_2)^2 \left(\dot{R}_1 + \dot{R}_2\right)}\right|_{t=0} \tag{A.2.21}$$

References

[1] Atsushi Toramaru. Numerical study of nucleation and growth of bubbles in viscous magmas. *Journal of Geophysical Research: Solid Earth*, 100:1913–1931, 2 1995.

[2] T. Shimano and S. Nakada. Vesiculation path of ascending magma in the 1983 and the 2000 eruptions of miyakejima volcano, japan. *Bulletin of Volcanology*, 68:549–566, 5 2006.

[3] C. Klug, K. Cashman, and C. Bacon. Structure and physical characteristics of pumice from the climactic eruption of mount mazama (crater lake), oregon. *Bulletin of Volcanology*, 64:486–501, 10 2002.

[4] Hélène Gaonac'h, Shaun Lovejoy, and Daniel Schertzer. Scaling vesicle distributions and volcanic eruptions. *Bulletin of Volcanology*, 67:350–357, 4 2005.

[5] Drok L Sahagian, Alfred T Anderson, and Brian Ward. Vold fi ology numerical model with natural examples. 1974:49–56, 1989.

[6] H. Gaonac'h, S. Lovejoy, J. Stix, and D. Scherzter. A scaling growth model for bubbles in basaltic lava flows. *Earth and Planetary Science Letters*, 1996.

[7] H Gaonac'h Ay, J Stix, and S Lovejoy. Scaling effects on vesicle shape, size and heterogeneity of lavas from mount etna, 1996.

[8] S. Lovejoy, H. Gaonac'h, and Daniel Schertzer. Bubble distributions and dynamics: The expansion-coalescence equation. *Journal of Geophysical Research: Solid Earth*, 109:1–16, 2004.

[9] Simona Mancini, Louis Forestier-Coste, Alain Burgisser, François James, and Jonathan Castro. An expansion-coalescence model to track gas bubble populations in magmas. *Journal of Volcanology and Geothermal Research*, 313:44–58, 2016.

[10] Michael Manga and H A Stone. Interactions between bubbles in magmas and lavas: effects of bubble deformation. *Journal of Volcanology and Geothermal Research*, 63:267–279, 1994.

[11] M. Masotta, H. Ni, and H. Keppler. In situ observations of bubble growth in basaltic, andesitic and rhyodacitic melts. *Contributions to Mineralogy and Petrology*, 167:1–14, 2014.

[12] Takafumi Maruishi and Atsushi Toramaru. Effect of bubble deformation on the coalescence of two ascending bubbles in a viscous liquid. *Physics of Fluids*, 34, 4 2022.

[13] Michael Manga and H A Stone. Collective hydrodynamics of deformable drops and bubbles in dilute low reynolds number suspensions. *Journal of Fluid Mechanics*, 300:231–263, 1995.

[14] David Saintillan, Eric S.G. Shaqfeh, and Eric Darve. The growth of concentration fluctuations in dilute dispersions of orientable and deformable particles under sedimentation. *Journal of Fluid Mechanics*, 553:347–388, 2006.

[15] J. Rallison. The deformation of small viscous drops and bubbles in shear flows. *Annual Review of Fluid Mechanics*, 16:45–66, 1 1984.

[16] S. Haber and G. Hetsroni. The dynamics of a deformable drop suspended in an unbounded stokes flow. *Journal of Fluid Mechanics*, 49:257–277, 9 1971.

[17] Michael Manga and H A Stone. Buoyancy-driven interactions between two deformable viscous drops. *Journal of Fluid Mechanics*, 256:647–683, 1993.

[18] Alexander Z. Zinchenko, Michael A. Rother, and Robert H. Davis. Cusping, capture, and breakup of interacting drops by a curvatureless boundary-integral algorithm. *Journal of Fluid Mechanics*, 391:249–292, 1999.

[19] C T Nguyen, H M Gonnermann, Y Chen, C Huber, A A Maiorano, A Gouldstone, and J Dufek. Film drainage and the lifetime of bubbles. *Geochem. Geophys. Geosyst*, 14:3616–3631, 2013.

[20] JOSEPH Kushner, MICHAEL A. Rother, and ROBERT H. Davis. Buoyancy-driven interactions of viscous drops with deforming interfaces. *Journal of Fluid Mechanics*, 446:253–269, 2001.

[21] A. Z. Zinchenko. Calculation of the effectiveness of gravitational coagulation of drops with allowance for internal circulation. *Journal of Applied Mathematics and Mechanics*, 46:58–65, 1982.

[22] Gesse A. Roure and Robert H. Davis. Modelling of particle capture by expanding droplets. *Journal of Fluid Mechanics*, 912, 2021.

[23] Gesse A. Roure, Jenna Trost, and Robert H. Davis. Particle capture by expanding droplets: effects of inner diffusion. *Journal of Fluid Mechanics*, 948, 10 2022.

[24] Man Hoi Lee. On the validity of the coagulation equation and the nature of runaway growth. *Icarus*, 143:74–86, 2000.

[25] F Xiao, T Yabe, and T Ito. I-12 computer physics communications, 1996.

[26] F Xiao, T Yabe, and T Ito. Constructing oscillation preventing scheme for advection equation by rational function, 1996.

[27] S. K. Friedlander and C. S. Wang. The self-preserving particle size distribution for coagulation by brownian motion. *Journal of Colloid And Interface Science*, 22:126–132, 1966.

[28] C. Hayashi and Y. Nakagawa. Size distribution of grains growing by thermal grain-grain collision. *Progress of Theoretical Physics*, 54:93–103, 1975.

[29] P. G.J. van Dongen and M. H. Ernst. Scaling solutions of smoluchowski's coagulation equation. *Journal of Statistical Physics*, 50:295–329, 1988.

[30] Cueille S and Sire C. Droplet nucleation and smoluchowski's equation with growth and injection of particles sté phane cueille and clé ment sire, 1998.

[31] N. G. Lensky, O. Navon, and V. Lyakhovsky. Bubble growth during decompression of magma: Experimental and theoretical investigation. *Journal of Volcanology and Geothermal Research*, 129:7–22, 2004.

[32] B. F. Houghton, J. Taddeucci, D. Andronico, H. M. Gonnermann, M. Pistolesi, M. R. Patrick, T. R. Orr, D. A. Swanson, M. Edmonds, D. Gaudin, R. J. Carey, and P. Scarlato. Stronger or longer: Discriminating between hawaiian and strombolian eruption styles. *Geology*, 44:163–166, 2 2016.

[33] E. A. Parfitt and L. Wilson. Explosive volcanic eruptions—ix. the transition between hawaiian‐style lava fountaining and strombolian explosive activity. *Geophysical Journal International*, 121:226–232, 1995.

[34] L. Wilson and J. W. Head. Ascent and eruption of basaltic magma on the earth and moon. *Journal of Geophysical Research*, 86:2971–3001, 1981.

[35] E. Bouche, S. Vergniolle, T. Staudacher, A. Nercessian, J. C. Delmont, M. Frogneux, F. Cartault, and A. Le Pichon. The role of large bubbles detected from acoustic measurements on the dynamics of erta 'ale lava lake (ethiopia). *Earth and Planetary Science Letters*, 295:37–48, 2010.